

Physicochemical and Antibacterial Properties of Bivalent Freeze and Furnace Dried Nanoscale Cerium Oxide

Neelam Iqbal

University of Leeds School of Process Environmental and Materials Engineering: University of Leeds School of Chemical and Process Engineering <https://orcid.org/0000-0002-2801-707X>

Antonios Anastasiou

University of Manchester Institute of Science and Technology: The University of Manchester

Zabeada Aslam

University of Leeds School of Process Environmental and Materials Engineering: University of Leeds School of Chemical and Process Engineering

Mostafa El Raif

University of Leeds School of Dentistry: Leeds Dental Institute

Thuy Do

University of Leeds School of Dentistry: Leeds Dental Institute

Peter Giannoudis

University of Leeds Faculty of Medicine and Health

Animesh Jha (✉ a.jha@leeds.ac.uk)

University of Leeds <https://orcid.org/0000-0003-3150-5645>

Research

Keywords: cerium oxide nanoparticles, antibacterial, antibiotic-free, oxidation states, bone infection

Posted Date: December 31st, 2020

DOI: <https://doi.org/10.21203/rs.3.rs-136744/v1>

License: © ⓘ This work is licensed under a Creative Commons Attribution 4.0 International License.

[Read Full License](#)

1. Introduction	1
2. Experimental	6
2.1 Reagents & Materials	6
2.2 Material Synthesis	6
2.2.1 Freeze Dried Cerium Oxide Nanoparticles	6
2.2.2 Furnace Dried Cerium Oxide Nanoparticles	7
2.3 Characterisation	8
2.3.1 Thermal Analysis	8
2.3.2 Fourier Transform Infrared (FTIR) and Ultraviolet-Visible (UV-Vis) Spectroscopy	8
2.3.3 X-ray Diffraction (XRPD)	9
2.3.4 Transmission Electron Microscopy (TEM)	9
2.3.5 X-ray Photoelectron Spectroscopy (XPS)	9
2.3.6 Surface Area	10
2.4 Bacterial Culture and Antibacterial Properties	10
2.4.1 Brain Heart Infusion Agar Plates and Broth	10
2.4.2 Growth of Bacterial Strains	11
2.4.3 Optical Density Measurements Without and With Nanoparticles	11
3. Results and Discussion	12
3.1 Characterisation	12
3.1.1 Thermal Analysis	12
3.1.2 Fourier Transform Infrared Spectroscopy	12
3.1.3 Ultraviolet-Visible Spectroscopy	13
3.1.4 X-ray Diffraction	14
3.1.5 Transmission Electron Microscopy	16
3.1.6 X-ray Photoelectron Spectroscopy	17
3.1.7 Electron Energy Loss Spectroscopy	19
3.2 Bacterial Growth	20
3.2.1 Optical Density Measurements with Nanoparticles	20
4. Conclusions	22
Declarations	23
References	26
Figures	31

Physicochemical and Antibacterial Properties of Bivalent Freeze and Furnace Dried Nanoscale Cerium Oxide

Neelam Iqbal¹, Antonios Anastasiou², Zabeada Aslam¹, Mostafa El-Raif³, Thuy Do³, Peter V Giannoudis⁴ and Animesh Jha^{1*}

¹School of Chemical and Processing Engineering, Woodhouse, University of Leeds, Leeds, LS2 9JT

²Department of Chemical Engineering and Analytical Science, University of Manchester, Manchester, M1 3AL

³School of Dentistry, Wellcome Trust Brenner Building, University of, Leeds LS9 7TF

⁴Leeds Institute of Rheumatic and Musculoskeletal Medicine, School of Medicine, University of Leeds, Leeds LS2 9JT

*Corresponding author e-mail address: **A.jha@leeds.ac.uk**

Abstract

Bone healing is a complex process, and if not managed, can lead to bacterial infections, non-union and compromised healing of bone. The broad overuse of antibiotics has led to the emergence of antibiotic-resistant bacteria. Due to the growing urgency to minimise the dependency on antibiotic drugs, alternative treatment strategies, including the use of nanoparticles, have attracted significant attention. Bivalent cerium oxide nanoparticles (Ce^{4+} and Ce^{3+}) synthesised via a hydroxide mediated approach were calcined at 280, 385 and 815 °C identified using the Simultaneous Thermal Analysis technique. The resulting nanoparticles were characterised using X-ray Powder Diffraction, Fourier Transform Infrared Spectroscopy, Ultraviolet-Visible Spectroscopy, Transmission Electron Microscopy, and Electron Energy Loss Spectroscopy. The antibacterial potential of cerium oxide nanoparticles corresponds to the particle size and the presence of oxygen vacancies in the fluorite crystal structure. The antibacterial efficacy of nanoparticles was characterised at concentrations of 50, 100 and 200 $\mu\text{g/ml}$ and tested against the following strains, *Escherichia coli*, *Staphylococcus epidermis* and *Pseudomonas aeruginosa* by determining the half-maximal inhibitory concentration (IC_{50}). The calcination temperature was found to affect the agglomeration tendency, particle size distribution and the ratio of $\text{Ce}^{3+}:\text{Ce}^{4+}$ oxidation states. The hydroxide mediated approach yielded spherical nanoparticles of ceria with particles size ranging from 4 nm to 53 nm. The freeze-dried bivalent nanoparticles exhibited $18.5 \pm 1.2 \%$, $10.5 \pm 4.4 \%$, and $13.8 \pm 5.8 \%$ increased antibacterial efficacy against *Escherichia coli*, *Pseudomonas aeruginosa* and *Staphylococcus epidermis*, respectively compared to nanoparticles consisting solely of Ce^{4+} ions, i.e. nanoparticles calcined at 815 °C.

Keywords: cerium oxide nanoparticles, antibacterial, antibiotic-free, oxidation states, bone infection.

1. Introduction

Bone infections are frequent due to the increasing incidence of trauma and elective surgeries (1-3). Sources of infectious bacteria include the operating room, surgical equipment, contaminated orthopaedic/medical device but also resident microbiota already present on the patient's skin (4). Epidemiological studies suggest between 2 and 5 % (5, 6) of all the implant-related procedures are likely to be further complicated due to post-operative infections leading to an increase in substantial health-related costs, prolonged hospitalisation, revision surgeries but also morbidity (7-9). The treatment of infection is complex involving parenteral or systemic drug administration and in extreme cases, debridement of bone and tissue due to compromised blood circulation (10). Drug administration for infection control uses a broad range of antibiotics which has led to the emergence of multidrug-resistant bacterial strains (8, 11). As a result, the treatment of diseases which were under control several years ago now require higher doses of multiple antibiotics, often leading to intolerable toxicity.

Contaminated surgical instruments or residual bacteria present on the implanted orthopaedic device introduces bacteria into the patient's body. Tissue and proteins in the blood gradually adsorb to the surface of the implanted device, as demonstrated extensively in the literature (7, 12-15). Bacteria in a planktonic state adheres to the adsorbed proteins and proliferates until a colony of bacteria is formed, enabling a change in the gene expression pattern. The genes responsible for the production of bacterial extracellular polymeric substances (EPS) are activated and expressed (12). The excretion of EPS further facilitates the exponential growth of bacteria leading to biofilm formation (7, 14, 15). Thus, the presence of a biofilm hinders the host's immune response and antibiotic delivery; hence biofilms are one of the major causes for the development of bacterial resistance (8).

The mechanism for bacterial resistance can be attributed to evolutionary processes taking place during antibiotic therapies and via horizontal gene transfer by (i) conjugations, (ii) transduction and (iii) transformation (i.e. commonly known as superbugs) (13). Antibiotics work by attacking at least three modes of targets; cell wall, translation mechanism and DNA replication mechanism. However, many bacteria have developed a resistant gene known as New Delhi Metallo-Beta-Lactamase-1 (NDM-1), which prevents the destruction of bacteria. Mechanisms of bacterial resistance include the expression of certain enzymes which can modify or destroy antibiotics, i.e. β -lactamases (16), modification of ribosomes and cell wall as shown with tetracycline and vancomycin resistance (7). Due to the growing urgency to minimise the dependency on antibiotic drugs, alternative treatment strategies, including the use of nanoparticles, have attracted significant attention as these types of particles manifest unique physicochemical properties. The unique properties are only apparent on the nanoscale, e.g. surface area to volume ratio, surface charge and oxidation state when compared with bulk counterparts (17). Several types of inorganic nanoparticles (ZnO, TiO₂, Ag) are emerging as novel antibacterial agents and proven their effectiveness for treating infectious diseases (18).

Antibacterial efficacy of nanoparticles is affected by factors such as the size, shape, surface charge and surface area to volume ratio (17). Nanoparticles size is essential with regards to biological functions as the morphological dimensions are comparable with (i) small biological molecules (1-10 nm), (ii) viruses (10-100 nm) and (iii) ability to attack biological entities without changing their functions (17). The antibacterial mechanism is likely to be attributed to their ability to enter biofilms; unlike antibiotics, nanoparticles directly attack the cell wall of bacteria by attaching via (i) electrostatic interaction, (ii) Van der Waals forces as well as (iii) receptor-ligand and hydrophobic interactions (8) disrupting the integrity of the bacterial cell wall leading to cell death (19).

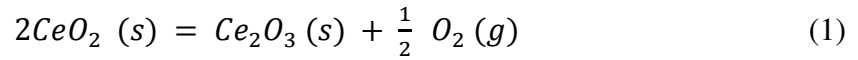
Nanoparticles can prevent bacteria from mutating via cell death; thus could replace or reduce the use of conventional antibiotics (20). The antibacterial properties of metal and metal oxide nanoparticles such as silver (21), copper (22), zinc oxide (23) and titanium dioxide (24) demonstrated to alter the metabolic activity of Gram-positive and negative bacteria (8). Zinc oxide nanoparticles are found to inhibit *Staphylococcus aureus*, whereas concentration-dependent silver nanoparticles exhibited antimicrobial activity against *Escherichia coli* and *Pseudomonas aeruginosa* (25). However, specific nanoparticles, i.e. silver, are toxic to host cells even at low doses despite exhibiting antibacterial properties (26). Nanosilver intraperitoneal injection and its dispersion through blood are found to adversely affect the lungs, liver, gastroenterological tract and brain tissues (27). For this reason, the use of silver in treating internal infections is now severely curtailed. Other studies have reported gold (28), magnesium oxide (29) and copper oxide (8, 30, 31) based nanoparticles prevented the formation of biofilm, which is linked to the high surface area-to-mass ratio, i.e. smaller sized less than 10 nm (7, 32). Additionally, triangular-shaped silver particles exhibited higher antibacterial properties as compared with spherical or rod-shaped nanoparticles (33).

Cerium oxide nanoparticles have attracted a great deal of interest as antibacterial agents due to the ability to cycle between the two valences states (Ce^{3+} and Ce^{4+}) leading to the formation of oxygen vacancies in the lattice. The apparent beneficial oxygen buffering capability enables the nanoparticles to act as a catalyst for both oxidation and reduction reactions (34); hence can manifest a unique antibacterial mechanism (20). The intrinsic bivalence of cerium oxide nanoparticles induces antioxidant capabilities (35) (catalytic oxidation and reduction) protecting the cells from oxidative stress, inflammation (36) and potential radiation damage (37). Nanoscale cerium oxide can mimic an antioxidant enzyme superoxide dismutase found

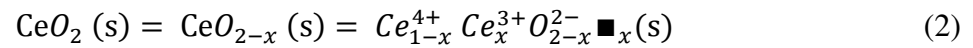
in all living cells (38). Superoxide dismutase, catalase and glutathione are considered the body's cellular defence as they catalyse the breakdown of potentially harmful oxygen molecules known as reactive oxygen species (ROS)/free radicals thus preventing tissue damage within the body. The primary role of antioxidants is to reduce excessive amounts of ROS/free radicals hence combating oxidative stress-related diseases (39). Nanoscale cerium presents relatively low or no toxicity to mammalian cells (40-43) and is proven to decrease catalysts of chronic inflammation via nanotherapeutics (36) as well as demonstrating the ability to enhance neuroprotection (44).

Cerium oxide nanoparticles exhibit pro-oxidative behaviour, depending on the environment, i.e. oxidative stress is induced, which is directed at bacteria (45). Conversely, several studies are concluding that there is no apparent antibacterial effect of cerium oxide nanoparticles (46, 47). However, other findings highlight possible adverse effects of the cerium oxide nanoparticles, where oxidative stress was induced in epithelial human lung cells (48). The range of conflicting data may be attributed to factors such as varying manufacturing processes, chemical solvents not entirely removed, irregular pH during production and increased calcination temperatures (49). The redox properties of cerium oxide nanoparticles can be tuned via materials preparation method, drying method, particle size, surface chemistry, particle shape and level of dopant materials (34). The drying method of nanoparticles is a vital aspect to consider as nanoparticles tend to agglomerate, which adversely affects the physicochemical properties of the particles (50). Thus, the procedures employed to evaluate the antimicrobial and antibacterial properties associated with cerium oxide nanoparticles may also make it challenging to form significant conclusions.

In the fluorite structure of cerium oxide, the redox equilibrium between the two valence states ($Ce^{3+}:Ce^{4+}$) may be explained by considering the reaction in the presence of oxygen gas, as shown in equation (1):



The intrinsic presence of oxygen vacancies in the CeO_2 crystal structure renders CeO_2 into a CeO_{2-x} non-stoichiometric oxide with 'x' vacant oxygen sites (51). The ratio of $Ce^{3+}:Ce^{4+}$ ionic states compensates against vacant oxygen sites and may be represented by the following equation:



In equation (2), the oxygen vacancy is shown by \blacksquare_x where x is the fractional value of vacant sites in the fluorite structure. Oxygen deficiencies in the fluorite crystalline lattice occur when the oxygen partial pressure is less than the value predicted value from equation (1) enabling the vacant oxygen sites to act as a sink for oxygen, an essential step in redox reaction equilibrium in the cerium-oxygen system.

In the present work, bivalent cerium oxide nanoparticles ($Ce^{4+}:Ce^{3+}$) have been selected due to their reported antibacterial and pharmaceutical properties as well as their potential to enhance vascularisation (52). The properties of three types of nanoscale cerium, i.e. commercial nanoparticles (RNP4), freeze-dried (FRNP) and calcined (C280, C385 and C815) are investigated. The management of bacterial growth is demonstrated by investigating the antibacterial efficacy of cerium oxide nanoparticles with varying $Ce^{4+}:Ce^{3+}$ ratio. Common Gram-negative and Gram-positive bacteria associated with orthopaedic infections, i.e.

Escherichia coli (-ve) (53, 54), *Pseudomonas aeruginosa* (-ve) (55, 56) and *Staphylococcus epidermis* (+ve) (4, 53, 57) were selected. The half-maximal inhibitory concentration (IC_{50}) was determined, corresponding to the reduction of bacterial growth by 50%.

2. Experimental

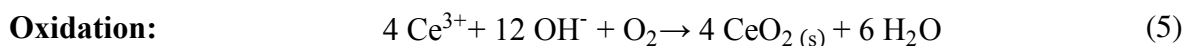
2.1 Reagents & Materials

Reagents and materials used for the preparation of cerium oxide nanoparticles were of analytical grade, i.e. cerium nitrate hexahydrate ($Ce(NO_3)_3 \cdot 6H_2O$) [Sigma-Aldrich, CAS: 10294-41-4], cerium (IV) oxide (CeO_2) [Sigma-Aldrich, CAS: 1306-38-3], cerium (III) nitrate ($CePO_4$) [Alfa Aesar, CAS: 13454-71-2] and sodium hydroxide (NaOH) [Sigma-Aldrich, CAS: 1310-73-2].

2.2 Material Synthesis

2.2.1 Freeze Dried Cerium Oxide Nanoparticles

The nanoparticles were synthesised via a hydroxide mediated method where Cerium Nitrate Hexahydrate ($Ce(NO_3)_3 \cdot 6H_2O$) was used as a precursor. Briefly, 10.85 g $Ce(NO_3)_3 \cdot 6H_2O_{(s)}$ was dissolved in 250 ml distilled water under continuous stirring for 20 minutes, resulting in a 0.1 M cerium solution (A). Then 0.3 M NaOH solution was added dropwise under continuous stirring to solution A at 50 °C for promoting hydrolysis of cerium oxide nanoparticles summarised via equations 3-5. The solution was covered with aluminium foil and left at 50 °C under continuous stirring for 24 hours. The nanoparticles were filtered and five times with distilled water and ethanol. The collected nanoparticles were frozen at -80 °C for 24 hours and then placed into a freeze drier for 24 hours.



2.2.2 Furnace Dried Cerium Oxide Nanoparticles

The hydroxide mediated synthesised cerium oxide nanoparticles were placed into a furnace at 80 °C for 24 hours for drying. Thermal analysis of the furnace dried powder was used to determine the optimal calcination temperature. All synthesised cerium oxide nanoparticles are presented in Table 1 with sample code names, corresponding formulas, and synthesis method.

Table 1 - Summary of commercial and synthesised nanoparticles with the post-synthesis cryo and thermal treatments.

Code	Description	Chemical Formula	Synthesis
RNP3	Cerium Phosphate	CeO ₄ P	Alfa Aesar, CAS: 13454-71-2
RNP4	Cerium Oxide	CeO ₂	Sigma-Aldrich, CAS: 1306-38-3
FRNP	Freeze Dried	-	Hydroxide mediated approach then freeze-dried
FUNP	Furnace Dried	-	Hydroxide mediated approach then dried @ 80°C
C280	Calcined @ 280°C	-	Heat treatment of FUNP (280°C, 2 hours)

C385	Calcined @ 385°C	-	Heat treatment of FUNP (385°C, 2 hours)
C815	Calcined @ 815°C	-	Heat treatment of FUNP (815°C, 2 hours)

2.3 Characterisation

2.3.1 Thermal Analysis

Reactions and phase changes of freeze-dried scaffolds were investigated using the Perkin Elmer STA 8000. The thermal experiments were carried out from 30 °C to 600 °C at a heating rate of 20 °C/min. The Perkin Elmer STA 8000, which was used to study the phase transformation and chemical reactions covered the temperature heating range from 30°C to 1000 °C. The thermal analysis characterisation of furnace dried ceria was essential for the optimisation of the calcination process without promoting the growth of nanoparticles. The isochronal heating rate of 20 °C min⁻¹ was used to determine the optimal calcination temperature for the furnace dried cerium oxide nanoparticles samples for comparative studies.

2.3.2 Fourier Transform Infrared (FTIR) and Ultraviolet-Visible (UV-Vis) Spectroscopy

The molecular vibration spectroscopic analysis of synthesised powders (FUNP, FRNP, C285, C385 and C815) were analysed and characterised by using the Vertex 70 FTIR spectrometer in the attenuated total reflection mode (ATR). The beam splitter used was KBr, and the light source used was a NIR lamp. Each sample was scanned 32 times in the 400 cm⁻¹ to 40000 cm⁻¹ range. The spectral resolution was 4 cm⁻¹. For the characterisation of the electronic absorption spectra of the nanoparticles, the PerkinElmer®, LAMDA 950 UV/VIS/NIR Spectrometer was used. A homogeneous clear suspension of nanoparticles in deionised water at various concentrations was used to collect the absorption spectrum between 190 nm and 600 nm.

2.3.3 X-ray Diffraction (XRPD)

A D8 X-ray powder diffractometer using the K_{α} radiation of Cu ($\lambda = 0.15406$ nm) was used to determine the crystalline structure of all prepared nanoparticles. The powder samples were analysed in the Bragg angle (2θ) scanning range of 10° to 80° at a scan speed of 5 seconds with a step size of 0.03° . The recorded patterns were analysed using the HighScore Plus software, and the Rietveld refinement was employed for peak shape and intensity analysis for ascertaining the crystallinity of powder sample.

2.3.4 Transmission Electron Microscopy (TEM)

For TEM analysis, the samples were prepared by ultrasonic dispersion of the nanoparticles in methanol after which several drops were placed onto holey carbon copper TEM grids. The particles suspended in methanol were then allowed to dry using a heat lamp. The Titan Themis Cubed 300 TEM operated at 300 kV with high brightness X-FEG and Supertwin objective lens, was used for the characterisation of the nanoscale size distribution and morphological analysis. The Bright field TEM images were collected using the Gatan OneView 16 Megapixel CMOS digital camera. Selected area electron diffraction (SAED) patterns, low magnification and dark-field (DF) TEM images were obtained for the analysis of the crystallinity of synthesised ceria. Electron energy loss spectroscopy (EELs) using the Gatan GIF Quantum ER imaging filter at low and high energy loss spectra were collected for the characterisation of the co-existence of the two oxidation states in the calcined nanoparticles.

2.3.5 X-ray Photoelectron Spectroscopy (XPS)

The nanoparticles (FRNP, FUNP, C280, C385 and C815) samples were prepared for XPS by sprinkling small amounts onto adhesive conductive carbon tape mounted on to the sample holders. The samples were sprayed with aerosol air to remove any loose particles before

analysis. The nanoparticles were then characterised using the UHV XPS with a SPEC Phoibos 150 analyser and a SPECS XR50-M. Samples surveys were taken at pass energy of 50Ev, and high-resolution scans were taken at 30Ev. The data collected were analysed using Prodigy, CASAxps and Originpro.

2.3.6 *Surface Area*

Micromeritics Tristar 3000 was used to characterise the Brunauer Emmett Teller (BET) surface area of the synthesised nanoparticles using the nitrogen absorption method in the powder bed. Measured amounts of nanoparticles in glass sample tubes were placed into the FlowPrep™ 060 where both heat and inert gas was applied to the samples for 30 minutes to remove any atmospheric contaminants, i.e. water and absorbed gas.

2.4 Bacterial Culture and Antibacterial Properties

The nanoparticles tested during the bacterial experiments were sterilised via autoclaving by suspending the particles in a Brain Heart Infusion (BHI) broth and once cooled were used within the hour. Optical density and viable count (in colony-forming units, CFUs) measurements were carried out to assess the antibacterial characteristics of the nanoparticles over 48 hours. An initial Optical Density OD₆₀₀ of 0.015 was selected (58) and was kept constant for all experiments to ensure reproducibility.

2.4.1 *Brain Heart Infusion Agar Plates and Broth*

Brain Heart Infusion (BHI) agar [Sigma Aldrich, BHI Agar #70138] plates [Sigma-Aldrich, BRAND® disposable petri dish with lid #BR452005] were prepared following the manufacturer's protocol. The solution was sterilised by autoclaving at 121 °C for 15 minutes. Once the agar solution had cooled, it was poured into a set of sterile agar plates under aseptic conditions which were left to solidify. The agar plates were then stored at < 4 °C until they

were required. The BHI broth [Sigma Aldrich, BHI Broth #53286] was prepared by dissolving 37 g of broth powder in 1 litre of distilled water and boiled to dissolve the medium completely. The broth was autoclaved at 121 °C for 15 minutes to sterilise and refrigerated at < 4 °C for future experiments.

2.4.2 Growth of Bacterial Strains

Bacterial stock cultures of *Escherichia coli*, *Staphylococcus epidermis* and *Pseudomonas aeruginosa* were procured from a stock 30 % glycerol solutions kept at –80 °C. Ten µl sterile loops were used to streak *Staphylococcus epidermis*, *Pseudomonas aeruginosa* and *Escherichia coli* onto Brain Heart Infusion (BHI) agar plates. Inoculated plates were incubated at 37 °C for 24 hours after which a single colony was picked from each bacterium type and grown in 25 ml of BHI broth in an incubator at 37 °C 150 rpm for 24 hours. This process enabled the production of fresh bacterial suspension for further use by inoculation.

2.4.3 Optical Density Measurements Without and With Nanoparticles

Optical density (OD) measurement is a widely used method to assess the number of growing bacteria in a culture; thus, the absorbance values of bacterial suspensions can be measured using a photometer (59). The initial optical densities of each bacterium type were measured using the Jenway 6305 UV/Visible Spectrophotometer at 600 nm (OD₆₀₀). The bacterium was diluted to an OD₆₀₀ of 0.015 (58, 60) using BHI broth to ensure reproducibility. Triplicate bacterial solutions for each bacterium were produced, and the growth rate without the addition of the nanoparticles was measured at 2, 4, 24 and 48 hours. To investigate the antibacterial properties of selected nanoparticles (FRNP, C385 and C815) various concentrations (50, 100, and 200 µg/ml) of sterilised nanoparticles suspended in BHI broth were added to the bacterial suspensions OD₆₀₀ of 0.015. The OD₆₀₀ was measured after 2, 4, 24, and 48 hours and compared

with the optical density measurements of bacterial suspensions containing no nanoparticles, the average values \pm SD are reported.

3. Results and Discussion

3.1 Characterisation

3.1.1 *Thermal Analysis*

Simultaneous Thermal Analysis (**Figure 1**) of FUNP nanoparticles revealed gradual weight loss from 100 °C due to the removal of trapped moisture and atmospheric gases, i.e. water and carbon dioxide (61). The three exothermic peaks (i) 280°C, (ii) 385°C and (iii) 815°C are likely to be associated with the combustion of organic residues, e.g. NaOH and C₂H₅OH (62) as calcination allows for the removal of any impurities leading to the formation of crystalline nanoparticles. No weight loss is observed above 600 °C, suggesting the formation of crystalline nanoparticles as confirmed by sample C815 X-ray diffraction pattern (**Figure 4**). Temperature plays a significant role with regards to nanoparticle structural changes, i.e. higher calcination temperatures often lead to larger nanoparticle sizes (63) but also affects the Ce³⁺ and Ce⁴⁺ ionic ratio. The literature mentions that antibacterial properties of nanoparticles are dependent upon ionic ratio, and particle size, i.e. the smaller the particle size, the better the overall antibacterial properties (64-66). Ostwald Ripening (62) or the coalescence of smaller particles (agglomeration) could lead to a temperature-dependent particle size increase. The structural changes occurring at the endothermic peaks are investigated by heat-treating the FUNP nanoparticles calcined at 280°C, 385°C and 815°C.

3.1.2 *Fourier Transform Infrared Spectroscopy*

FTIR spectra for the synthesised cerium oxide nanoparticles are shown in **Figure 2**. The bands related to Ce-O stretching vibrations are located in the region of 500 cm⁻¹ to 750 cm⁻¹. As the

heat treatment of the cerium oxide nanoparticles increases, the presence of the Ce-O vibrational band broadens, which is likely related to an increase of Ce⁴⁺ and is also confirmed from the Electron Energy Loss Spectroscopy (EELs) results. Atmospheric CO₂ is readily trapped during the nanoparticles synthesis; hence the corresponding peaks are observed in the 750 cm⁻¹ to 650 cm⁻¹ regions. The peaks located around 2050 cm⁻¹ are attributed to vibrational bending of C-H bands corresponding to incorporated surfactant residuals which reduce as the calcination temperature increases from 280 °C to 815 °C. The broad reflectance peak at 4000 cm⁻¹ to 3500 cm⁻¹ relates to the O-H stretching, which diminishes as the calcination temperature increases thus, indicating the removal of water molecules in the synthesised calcined samples (C280, C385 and C815). Similar FTIR results relating to cerium oxide nanoparticles are described in the literature (43, 67-69).

3.1.3 Ultraviolet-Visible Spectroscopy

Absorbance spectra for the cerium oxide nanoparticles are shown in **Figure 3**, where the maximum absorbance is located in the 210 nm regions. The electronic behaviour, oxygen defects, particle size and the bivalence of the cerium oxide nanoparticles affects the optical properties of the nanoparticles. Also, an increase in the heat treatment temperatures likely affected the size distribution of the cerium oxide nanoparticles as confirmed from TEM images analysis depicted in **Figure 5**. Bandgap energies E_g of the synthesised nanoparticles are investigated from the absorption spectra and calculated via The Tauc equation (equation 4) which determines the bandgap energy between valence and conduction bands of the nanoparticles spectrophotometrically:

$$\alpha h \nu = A (h \nu - E_g)^{0.5} \quad (6)$$

With A being the absorption, α refers to the absorption coefficient, $h\nu$ is the photon energy ($1240/\lambda$), and E_g relates to the bandgap. Therefore, the bandgap energies are determined from the x-axis intersections of $(\alpha h\nu)^2$ vs $h\nu$ plots (**Figure 3 (b-e)**). The absorption maxima for samples calcined at 280 °C, 385 °C and 815 °C exhibited a slight blue shift as absorption shifted to smaller wavelengths for calcined nanoparticles (C280, C385 and C815) (70). The blue shift implies that the optical band gap energy decreases as the nanoparticle sizes increase, which has also been confirmed by other researchers (71, 72). The direct optical band gap energies for the FRNP, FUNP, C280, C385 and C815 nanoparticles were found to be 5.6 eV, 5.5 eV, 5.2 eV, 4.7 and 3.4 eV respectively. The difference in the band energies is related to the presence of different oxidation states (Ce^{3+} and Ce^{4+}) on the outer nanoparticles' surfaces where the $Ce^{3+}:Ce^{4+}$ ratio is known to be affected by oxygen vacancies and surface defects (63, 73, 74).

3.1.4 X-ray Diffraction

The crystalline structure, i.e. composition, crystallite size and microstrain in the nanoparticles have been determined from the diffraction patterns (**Figure 4**). The XRD diffraction spectra for the synthesised nanoparticles exhibit eight major characterisation peaks located at 28.49, 33.00, 47.38, 56.12, 58.96, 69.45, 76.51 and 78.89° which corresponds to (111), (200), (220), (311), (222), (400), (331) and (420) Miller Indices respectively. The synthesised nanoparticles are single phased material, and the analysed structure agrees with the phase fluorite type CeO_2 JCPDS 00-067-0123 reference with a lattice parameter of 0.5423 nm. Notably, the (111) peaks shift to slightly higher 2θ values with increasing calcination temperatures, which suggests that the crystalline lattice dimensions are decreasing due to the removal of crystal lattice expansions resulting from nanoparticles coarsening. The intensities of the calcined nanoparticles increased with increasing calcination temperatures from 280 to 815 °C and, may be attributed to the improvement in the overall crystallinity and lattice strain arising from oxygen deficiency; the

data are compared in **Table 2**. Consequently, the full width at half maximum (FWHM) of XRD peaks decreased as the crystallinity of the nanoparticles increased with temperature. The reduction of FWHM peaks confirms that the calcination temperature affects the size and morphology of synthesised nanoparticles.

Table 2 - XRD data obtained from prepared nanoparticles, crystallite sizes were calculated via Scherrer and Williamson-Hall method.

Sample	Lattice Cell Parameter (Å)	Unit Cell Volume (Å ³)	BET Surface Area (m ² /g)	<i>Scherrer Method</i>	<i>Williamson- Hall Method</i>
				Crystallite Size (nm)	Crystallite Size (nm) Error: ×10 ⁻²
RNP4	5.41	158.73	36.72 ± 0.14	21.56 ± 6.47	16.25 ± 0.09
FRNP	5.42	159.52	71.63 ± 0.47	4.29 ± 1.29	5.38 ± 1.37
FUNP	5.40	158.16	36.40 ± 0.15	6.70 ± 2.01	8.09 ± 0.42
C280	5.41	158.37	35.40 ± 0.11	6.59 ± 1.97	8.48 ± 0.69
C385	5.39	157.37	46.37 ± 0.15	7.87 ± 2.37	10.69 ± 0.70
C815	5.37	155.52	4.27 ± 0.04	32.59 ± 9.78	45.31 ± 0.22

The interplanar spacing 'd' was calculated via Bragg's equation (equation 7) and the lattice cell parameter 'a' are determined for all samples using the following formula:

$$a = \frac{d}{(h^2 + k^2 + l^2)^{1/2}} \quad (7)$$

where 'a' refers to the FCC lattice parameter, 'd' corresponds to the crystalline face spacing and 'hkl' are the crystalline face indexes. The results are displayed in Table 2. The comparison of the crystallite sizes determined via the Scherrer and Williamson-Hall methods are also displayed in **Table 2**, where significant differences are observed between the values. The crystallite size noticeably increases with increasing calcination temperature, which is consistent with increasing particles size as confirmed from TEM analysis in **Figure 5** and also by the decreasing Brunauer Emmett Teller (BET) surface area results as displayed in **Table 2**. The intensities of the calcined nanoparticles increased with increasing calcination temperatures from 280 °C to 815 °C and can be attributed to crystallinity improvement of the nanoparticles confirmed from crystallite measurements displayed in **Table 2**. Consequently, the full width at half maximum (FWHM) of XRD peaks decreased as the crystallinity of the nanoparticles increased with temperature; hence the reduction of FWHM peaks confirm that the calcination temperature affects the size and morphology of synthesised nanoparticles.

3.1.5 Transmission Electron Microscopy

The majority of synthesised nanoparticles are spherical except RNP4 and the C815 nanoparticles. The smaller the size of the nanoparticles, the higher the agglomeration thus makes it difficult to observe individual particles. The particles size for RNP4, FRNP, FUNP, C280, C385 and C815 deduced from High-Resolution TEM (HRTEM) images were estimated to be 25, 4, 6, 8, 11 and 53 nm respectively. The three principle low index planes for nanoparticles are (111), (110) and (100). The (111) planes for the FUNP nanoparticles are observed in the HRTEM image (**Figure 5g**), and the calculated d-spacing values are displayed

in **Table 3**. The presence of lattice fringes is an indication of the crystalline nature of the synthesised nanoparticles. The Selected Area Electron Diffraction (SAED) patterns for all samples except RNP4 and C815 nanoparticles depict continuous ring patterns (**Figure 5h**). The presence of discrete rings is an indication of the polycrystalline structure of the nanoparticles but also the relatively small size of the nanoparticles. All the obtained SAED rings are in good agreement with the XRD diffraction patterns, confirming the fluorite structure.

Table 3 - Calculated d Spacing by (i) Bragg Equation, (ii) HRTEM images, (iii) From the (111) face index of SAED Transmission Electron Microscopy Diffraction Images.

Sample	Bragg Equation (nm)	Interplanar Spacing (nm)	Crystalline Face Index (nm) Error: $\times 10^{-3}$
RNP4	0.3126	0.3629	0.3225 ± 6.450
FRNP	0.3131	0.3423	0.3205 ± 6.410
FUNP	0.3122	0.3457	0.3196 ± 6.392
C280	0.3124	0.3630	0.3191 ± 6.382
C385	0.3117	0.3084	0.3216 ± 6.432
C815	0.3105	0.3249	0.3229 ± 6.458

3.1.6 X-ray Photoelectron Spectroscopy

The XPS measurements revealed significant differences in surface chemistry of the synthesised nanoparticles likely related to the drying method (furnace or freeze-drying) and calcination temperatures. It should be noted that XPS analyses the surface charge of the nanoparticles, whereas EELS analyses' the subsurface thus, is likely to differ regarding the $Ce^{3+}:Ce^{4+}$ ratio.

Table 4 displays the Ce 3d data for the FRNP, FUNP, C280, C385 and C815 cerium oxide nanoparticles. The spin-orbit doublet peaks associated with all the Ce 3d spectrums are **Ce 3d_{5/2}** located between ~870 eV to 895 eV, and **Ce 3d_{3/2}** located between ~895 eV to 915 eV. Additionally, multiple shake-up and shake-down satellite peaks are also present (75). The XPS spectra indicate the co-existence of Ce³⁺ and Ce⁴⁺ due to the presence of satellite peaks linked to each oxidation state. **Table 4** displays the XPS data regarding the energy peaks of the synthesised nanoparticles. Analysing the XPS measurements for the FRNP nanoparticles, the highest binding Ce 3d energy peaks u''' (921.4) and v''' (903.1) which correspond to the Ce⁴⁺ valence state from the Ce(3d⁹ 4f⁰) O(2p⁶) final states (76). The remaining four lower energy peaks i.e., u (906.1), v (887.3), u'' (910.3) and v'' (892.4) are attributed to the mixing of Ce(3d⁹ 4f²) O(2p⁴) and Ce(3d⁹ 4f¹) O(2p⁵) final states. Contributions related to the Ce³⁺ valence are labelled as u⁰ (905.5), v⁰ (882.1), u' (909.1) and v' (890.2) where the peaks are due to the mixing of Ce(3d⁹ 4f¹) O(2p⁶) and Ce(3d⁹ 4f²) O(2p⁵) final states (76-79). Increasing the calcination temperature caused a reduction of the Ce³⁺ doublet peaks (u', v', u⁰ and v⁰) suggesting a reduction of the Ce³⁺ ions with increasing heat treatment, similar results were obtained by other researchers (76).

Table 4 - XPS peak data for synthesis cerium oxide nanoparticles (FRNP, FUNP, C280, C385 and C815).

		FRNP	FUNP	C280	C385	C815
		(eV)	(eV)	(eV)	(eV)	(eV)
Ce⁴⁺	u	906.1	905.9	911.1	911.6	903.9
	v	887.3	887.2	891.8	891.7	885.1
	u''	910.3	912.2	915.8	916.2	909.8
	v''	892.4	892.2	897.3	896.7	890.9

	u'''	921.4	920.9	926.1	925.5	918.9
	v'''	903.1	903.2	908.1	908.2	900.9
Ce³⁺	u ⁰	905.5	905.2	904.9	904.7	903.1
	v ⁰	882.1	881.9	881.7	881.8	878.7
	u'	909.1	908.9	908.1	907.6	906.1
	v'	890.2	893.4	894.3	897.1	887.9

3.1.7 Electron Energy Loss Spectroscopy

Cerium oxide is electropositive and can exist in two oxidation modes, i.e. Ce³⁺ and Ce⁴⁺. The EELs measurements were acquired by rastering the beam across several locations for each nanoparticle sample. EELS spectra from two controls (Ce³⁺ and Ce⁴⁺) and five synthesised nanoparticles are shown in **Figure 6**. In each case, the background was removed, and Fourier-Ratio Deconvolution routines were applied prior to fitting. From the EELs spectra, the Ce M_{4,5} edges of FRNP, FUNP, C280, C385 and C815 spectra are shown where the black lines represent the sample data, the red lines represent the Ce⁴⁺ ion spectra, and the grey lines represent the Ce³⁺ ion spectra.

It is evident as the size of the nanoparticles increases for calcined samples the Ce³⁺:Ce⁴⁺ ratio decreases as the C815 sample contains 95 % majority of Ce⁴⁺ ions. The presence Ce⁴⁺ in the FRNP, FUNP, C280 and C385 is 37 %, 46 %, 30 %, and 67 % respectively. The stability of the Ce³⁺ ions diminishes with increasing temperatures, and this is related to the occupation of the oxygen vacancies in the fluorite structure in the presence of oxygen gas present in the air during the heat treatment. However, not all the oxygen vacancies are filled, thus leading to a variation in the Ce³⁺:Ce⁴⁺ ratio. The obtained results confirm that the Ce³⁺:Ce⁴⁺ ratio is temperature-dependent; therefore, the optimal calcination temperature must be characterised

to ensure optimal $Ce^{3+}:Ce^{4+}$, which provides the highest antibacterial efficacy. Based on the XPS and EELs results, the FRNP, C385 and C815 nanoparticles are selected due to the range of particle size and $Ce^{3+}:Ce^{4+}$ ratio to be further investigated.

3.2 Bacterial Growth

3.2.1 Optical Density Measurements with Nanoparticles

To investigate the antibacterial properties of nanoparticles with varying $Ce^{3+}:Ce^{4+}$ ratio and particle size distribution, FRNP, C385 and C815 nanoparticles were selected. We found all three types of nanoparticles exhibited antibacterial properties against Gram-positive and Gram-negative bacteria. However, the greatest antibacterial activity was observed against Gram-negative bacteria for the highest FRNP concentration (200 $\mu\text{g/ml}$) $38.8 \pm 6.4 \%$ reduction was observed against *Escherichia coli*. In contrast, a reduction of $28.7 \pm 10.2 \%$ was observed against *Pseudomonas aeruginosa* after 48 hours of incubation (**Figure 7**). The C385 nanoparticles exhibited $33.5 \pm 5.8 \%$, $20.7 \pm 8.1 \%$ and $13.9 \pm 1.1 \%$ reduction of *Escherichia coli*, *Pseudomonas aeruginosa* and *Staphylococcus epidermidis*, respectively. The lowest antibacterial activity was observed for C815 nanoparticles with $20.3 \pm 7.6 \%$, $18.2 \pm 5.8 \%$ and $6.4 \pm 9.9 \%$ bacterial reduction expressed against *Escherichia coli*, *Pseudomonas aeruginosa* and *Staphylococcus epidermidis*, respectively. The FRNP nanoparticles exhibited enhanced antibacterial efficacy compared to the C385, and C815 nanoparticles likely attributed to the high surface area to volume ratio and increased Ce^{3+} ions. Smaller sized cerium oxide nanoparticles appear more non-stoichiometric with respect oxygen, which proportionately increases the number of Ce^{3+} sites for facilitating the sites for redox reactions.

The nanoparticles size and the ratio of oxidation states ($Ce^{3+}:Ce^{4+}$) plays a significant role with regards to the antibacterial efficacy of cerium oxide nanoparticles. The primary antibacterial

mechanism for cerium oxide nanoparticles is attributed to direct contact between the nanoparticles and the bacterial membranes. Positively charged nanoparticles adsorb to the negatively charged bacterial membranes through electrostatic interaction and alter the viscosity and integrity of bacterial membranes. The disruption can cause the transport exchange proteins located on the bacterial membranes to become inactive, leading to disruption of bacterial cellular activity. Additionally, nanoscale cerium oxide can enter through the inactive transport exchange proteins and deactivate the bacterial enzymes by generating Reactive Oxidative Species (ROS). The ROS can cause damage to the plasmids containing DNA/RNA and ribosomes, leading to bacterial cell death (66). Several studies also found cerium oxide exhibited cytotoxic (19) and induced toxicity against *Escherichia coli* (19, 80). Reduction of bacterial growth has been observed for coated nanoscale ceria which inhibited 50 % *Pseudomonas aeruginosa* growth (81). Furthermore; cerium oxide nanoparticles have also exhibited moderate inhibitive activity against *Escherichia coli* and *Bacillus subtilis* (82-84).

The half-maximal inhibitory concentrations (IC_{50}) calculated from linear regression models are shown in **Table 5**. It is clear smaller sized nanoparticles, i.e. < 10 nm exhibit improved overall antibacterial efficacy against both Gram-positive and Gram-negative bacteria. The nanoparticles presented enhanced antibacterial activity against the Gram-negative bacteria, i.e. *Escherichia coli* and *Pseudomonas aeruginosa*, which is likely to be attributed to the structure of the bacterial cell wall. The cell wall of Gram-positive bacteria, e.g. *Staphylococcus epidermidis*, is composed of a relatively thick continuous peptidoglycan containing peptides and linear polysaccharide chains that is difficult for the nanoparticles to penetrate. However, the cell wall of Gram-negative bacteria is composed of a thin layer of peptidoglycan with a lipopolysaccharide surrounding the bacteria. Therefore allowing the nanoparticles to cause

more damage Gram-negative bacterial cell walls resulting in cell lysis, other studies (85, 86) also found similar results.

Table 5 - The half-maximal inhibitory concentration (IC₅₀) values of FRNP, RNP4 and C815 tested with *Escherichia coli*, *Pseudomonas aeruginosa* and *Staphylococcus epidermidis*.

IC ₅₀	<i>E.coli</i>	<i>P.aeruginosa</i>	<i>S.epidermis</i>
FRNP µg/ml	340 ± 4.0	558 ± 3.9	580 ± 4.6
C385 µg/ml	365 ± 6.6	619 ± 5.2	741 ± 5.6
C815 µg/ml	563 ± 8.2	663 ± 9.4	785 ± 5.8

4. Conclusions

We have demonstrated the successful synthesis of cerium oxide nanoparticles (4 nm to 53 nm) as confirmed from the XRD and TEM analysis. The drying method (i.e. freeze-drying or furnace drying) and calcination temperature significantly affected the physicochemical properties, i.e. size, shape, agglomeration and the oxidation ratio Ce³⁺:Ce⁴⁺. Increased calcination temperatures from 280 °C to 815 °C caused the size of the synthesised nanoparticles to increase; the average particle size grew by eight times 280 °C to 815 °C (C815) when compared with FRNP nanoparticles. The synthesised cerium oxide nanoparticles exhibited agglomeration, causing a lack of individual particles as confirmed from the TEM analysis, which would have negatively impacted the antibacterial potential. Two oxidation states were detected for FRNP, FUNP, C280, C385 and C815 cerium oxide nanoparticles. However, with increasing calcination temperatures, the Ce³⁺:Ce⁴⁺ ratio reduced where the nanoparticles calcined at 815 °C consisted of only 5 % of Ce³⁺ ions with the remaining existing as Ce⁴⁺. The

antibacterial properties of nanoparticles are dependent upon two main factors, (i) the type of bacteria and (ii) the physicochemical properties of the nanoparticles.

The FRNP, C385 and C815 nanoparticles all exhibited antibacterial properties against *Escherichia coli*, *Pseudomonas aeruginosa* and *Staphylococcus epidermis*. The FRNP nanoparticles presented significant antibacterial efficacy as compared to the larger size C385 and C815 nanoparticles. Particles size influences the antibacterial potential, where relatively small-sized particles cerium oxide nanoparticles (< 10 nm) can cause more damage to bacteria compared to larger particle sizes. The Ce³⁺:Ce⁴⁺ ratio also affected the antibacterial properties of the cerium oxide nanoparticles; the FRNP nanoparticles presented greater Ce³⁺ as compared to Ce⁴⁺, which led to enhanced antibacterial properties compared to the C385 and C815 nanoparticles. Additionally, improved antibacterial efficacy was observed towards *Escherichia coli* and *Pseudomonas aeruginosa* as compared to *Staphylococcus epidermis*. The reduced antibacterial potential against Gram-positive bacteria, e.g. *Staphylococcus epidermis* is attributed to the structural difference in thickness between Gram-positive and Gram-negative bacterial cell walls. As expected, the half-maximal inhibitory concentrations (IC₅₀) to reduce bacterial growth by 50 % were found to be lower for FRNP compared with the C385 and C815 nanoparticles.

Declarations

Ethics approval and consent to participate

Not applicable

Consent for publication

Not applicable

Availability of data and materials

The datasets used and/or analysed during the current study are available from the corresponding author on reasonable request.

Competing interests

The authors declare that they have no competing interests.

Funding

This work was funded by The Engineering and Physical Sciences Research Council (EPSRC), project reference number 1787225.

Authors' contributions

NI synthesised, characterised and tested the cerium oxide nanoparticles. ZA conducted TEM, EELS and SAED nanoparticles data collection. The bacteria-related experiments were performed by NI with guidance from MER and TD. The preparation of the manuscript consisted of contributions from NI, AA, and AJ.

Acknowledgements

The authors would like to acknowledge Mr Mohammed Javed, Dr Ben Douglas and Dr Simon Strafford for the laboratory support, Mr Stuart Micklethwaite for SEM support and Ms Vasiliki C Panagiotopoulou for proofreading support at the University of Leeds. Microbiology laboratory support was provided by Dr Emaan Alsubhe and Mr Sandeep Kumar at the School of Dentistry, University of Leeds.

List of symbols

BET	Brunauer Emmett Teller
BHI	Brain heart infusion
C280	Cerium oxide nanoparticles calcined at 280 °C
C385	Cerium oxide nanoparticles calcined at 385 °C
C815	Cerium oxide nanoparticles calcined at 815 °C
EELs	Electron Energy Loss Spectroscopy
FRNP	Freeze-dried cerium oxide nanoparticles
FTIR	Fourier Transform Infrared Spectroscopy
FUNP	Furnace-dried cerium oxide nanoparticles calcined at 280 °C
FWHM	Full width half maximum
HRTEM	High-Resolution Transmission Electron Microscopy
IC ₅₀	Half-maximal inhibitory concentrations
OD	Optical density
RNP4	Commercial cerium oxide nanoparticles
ROS	Reactive oxygen species
SAED	Selected Area Electron Diffraction
STA	Simultaneous Thermal Analysis
TEM	Transmission Electron Microscopy
UV-Vis	Ultraviolet-Visible Spectroscopy
XRPD	X-ray Powder Spectroscopy

References

1. Pulcini C, Couadau T, Bernard E, Lorthat-Jacob A, Bauer T, Cua E, et al. Adverse effects of parenteral antimicrobial therapy for chronic bone infections. *European Journal of Clinical Microbiology & Infectious Diseases*. 2008;27(12):1227-32.
2. Lew DP, Waldvogel FA. Osteomyelitis. *The Lancet*. 2004;364(9431):369-79.
3. Bernard L, Hoffmeyer P, Assal M, Vaudaux P, Schrenzel J, Lew D. Trends in the treatment of orthopaedic prosthetic infections. *Journal of Antimicrobial Chemotherapy*. 2004;53(2):127-9.
4. Ribeiro M, Monteiro FJ, Ferraz MP. Infection of orthopedic implants with emphasis on bacterial adhesion process and techniques used in studying bacterial-material interactions. *Biomater*. 2012;2(4):176-94.
5. Johnson CT, Garcia AJ. Scaffold-based anti-infection strategies in bone repair. *Annals of biomedical engineering*. 2015;43(3):515-28.
6. Anastasiou AD, Nerantzaki M, Gounari E, Duggal MS, Giannoudis PV, Jha A, et al. Antibacterial properties and regenerative potential of Sr(2+) and Ce(3+) doped fluorapatites; a potential solution for peri-implantitis. *Sci Rep*. 2019;9(1):14469.
7. Knetsch MLW, Koole LH. New Strategies in the Development of Antimicrobial Coatings: The Example of Increasing Usage of Silver and Silver Nanoparticles. *Polymers*. 2011;3(1):340.
8. Wang L, Hu C, Shao L. The antimicrobial activity of nanoparticles: present situation and prospects for the future. *International journal of nanomedicine*. 2017;12:1227-49.
9. Holmes NE, Turnidge JD, Munchhof WJ, Robinson JO, Korman TM, O'Sullivan MVN, et al. Genetic and molecular predictors of high vancomycin MIC in *Staphylococcus aureus* bacteremia isolates. *Journal of clinical microbiology*. 2014;52(9):3384-93.
10. Parsons B, Strauss E. Surgical management of chronic osteomyelitis. *The American Journal of Surgery*. 2004;188(1):57-66.
11. Anastasiou AD, Thomson CL, Hussain SA, Edwards TJ, Strafford S, Malinowski M, et al. Sintering of calcium phosphates with a femtosecond pulsed laser for hard tissue engineering. *Materials and Design*. 2016;101:346-54.
12. Mahmoudi M, Serpooshan V. Silver-Coated Engineered Magnetic Nanoparticles Are Promising for the Success in the Fight against Antibacterial Resistance Threat 2012. 2656-64 p.
13. Qiu Z, Yu Y, Chen Z, Jin M, Yang D, Zhao Z, et al. Nanoalumina promotes the horizontal transfer of multiresistance genes mediated by plasmids across genera. *Proceedings of the National Academy of Sciences of the United States of America*. 2012;109(13):4944-9.
14. Høiby N, Bjarnsholt T, Givskov M, Molin S, Ciofu O. Antibiotic resistance of bacterial biofilms. *Int J Antimicrob Agents*. 2010;35(4):322-32.
15. Hall-Stoodley L, Stoodley P. Evolving concepts in biofilm infections. *Cell Microbiol*. 2009;11(7):1034-43.
16. Poole K. Mechanisms of bacterial biocide and antibiotic resistance. *Journal of applied microbiology*. 2002;92 Suppl:55s-64s.
17. Raza MA, Kanwal Z, Rauf A, Sabri AN, Riaz S, Naseem S. Size- and Shape-Dependent Antibacterial Studies of Silver Nanoparticles Synthesized by Wet Chemical Routes. *Nanomaterials (Basel, Switzerland)*. 2016;6(4):74.
18. Hajipour MJ, Fromm KM, Ashkarran AA, Jimenez de Aberasturi D, de Larramendi IR, Rojo T, et al. Antibacterial properties of nanoparticles. *Trends in biotechnology*. 2012;30(10):499-511.

19. Thill A, Zeyons O, Spalla O, Chauvat F, Rose J, Auffan M, et al. Cytotoxicity of CeO₂ nanoparticles for Escherichia coli. Physico-chemical insight of the cytotoxicity mechanism. *Environmental science & technology*. 2006;40(19):6151-6.
20. Zhang M, Zhang C, Zhai X, Luo F, Du Y, Yan C. Antibacterial mechanism and activity of cerium oxide nanoparticles. *Science China Materials*. 2019;62(11):1727-39.
21. Shrivastava S, Bera T, Roy A, Singh G, Ramachandrarao P, Dash D. Characterization of enhanced antibacterial effects of novel silver nanoparticles. *Nanotechnology*. 2007;18(22):225103.
22. Usman MS, El Zowalaty ME, Shamel K, Zainuddin N, Salama M, Ibrahim NA. Synthesis, characterization, and antimicrobial properties of copper nanoparticles. *International journal of nanomedicine*. 2013;8:4467-79.
23. Jones N, Ray B, Ranjit KT, Manna AC. Antibacterial activity of ZnO nanoparticle suspensions on a broad spectrum of microorganisms. *FEMS Microbiol Lett*. 2008;279(1):71-6.
24. Cho M, Chung H, Choi W, Yoon J. Linear correlation between inactivation of E. coli and OH radical concentration in TiO₂ photocatalytic disinfection. *Water Res*. 2004;38(4):1069-77.
25. Ramalingam B, Parandhaman T, Das SK. Antibacterial Effects of Biosynthesized Silver Nanoparticles on Surface Ultrastructure and Nanomechanical Properties of Gram-Negative Bacteria viz. Escherichia coli and Pseudomonas aeruginosa. *ACS applied materials & interfaces*. 2016;8(7):4963-76.
26. AshaRani PV, Low Kah Mun G, Hande MP, Valiyaveetil S. Cytotoxicity and Genotoxicity of Silver Nanoparticles in Human Cells. *ACS Nano*. 2009;3(2):279-90.
27. Johnston HJ, Hutchison G, Christensen FM, Peters S, Hankin S, Stone V. A review of the in vivo and in vitro toxicity of silver and gold particulates: Particle attributes and biological mechanisms responsible for the observed toxicity. *Critical Reviews in Toxicology*. 2010;40(4):328-46.
28. Shareena Dasari TP, Zhang Y, Yu H. Antibacterial Activity and Cytotoxicity of Gold (I) and (III) Ions and Gold Nanoparticles. *Biochem Pharmacol (Los Angel)*. 2015;4(6):199.
29. Sawai J, Kojima H, Igarashi H, Hashimoto A, Shoji S, Sawaki T, et al. Antibacterial characteristics of magnesium oxide powder. *World Journal of Microbiology and Biotechnology*. 2000;16(2):187-94.
30. Qing Ya, Cheng L, Li R, Liu G, Zhang Y, Tang X, et al. Potential antibacterial mechanism of silver nanoparticles and the optimization of orthopedic implants by advanced modification technologies. *International journal of nanomedicine*. 2018;13:3311-27.
31. Dong Y, Zhu H, Shen Y, Zhang W, Zhang L. Antibacterial activity of silver nanoparticles of different particle size against Vibrio Natriegens. *PLOS ONE*. 2019;14(9):e0222322.
32. Wang L, Hu C, Shao L. The antimicrobial activity of nanoparticles: Present situation and prospects for the future. *International Journal of Nanomedicine*. 2017;Volume 12:1227-49.
33. Pal S, Tak YK, Song JM. Does the Antibacterial Activity of Silver Nanoparticles Depend on the Shape of the Nanoparticle? A Study of the Gram-Negative Bacterium & Escherichia coli. *Applied and Environmental Microbiology*. 2007;73(6):1712.
34. Reed K, Cormack A, Kulkarni A, Mayton M, Sayle D, Klaessig F, et al. Exploring the properties and applications of nanoceria: is there still plenty of room at the bottom? *Environmental Science: Nano*. 2014;1(5):390-405.
35. Lv G, Wang Y, Liu R, Sun L, Huang Y, Yan C. The application of nanoceria in the bio-antioxidation. *Scientia Sinica Chimica*. 2013;43:1309.

36. Hirst SM, Karakoti AS, Tyler RD, Sriranganathan N, Seal S, Reilly CM. Anti-inflammatory Properties of Cerium Oxide Nanoparticles. *Small*. 2009;5(24):2848-56.
37. Perez JM, Asati A, Nath S, Kaittanis C. Synthesis of biocompatible dextran-coated nanoceria with pH-dependent antioxidant properties. *Small*. 2008;4(5):552-6.
38. Korsvik C, Patil S, Seal S, Self WT. Superoxide dismutase mimetic properties exhibited by vacancy engineered ceria nanoparticles. *Chemical Communications*. 2007(10):1056-8.
39. Celardo I, Pedersen JZ, Traversa E, Ghibelli L. Pharmacological potential of cerium oxide nanoparticles. *Nanoscale*. 2011;3(4):1411-20.
40. Tarnuzzer R, Colon J, Patil S, Seal S. Vacancy Engineered Ceria Nanostructures for Protection from Radiation-Induced Cellular Damage. *Nano letters*. 2006;5:2573-7.
41. Tsai YY, Oca-Cossio J, Agering K, Simpson NE, Atkinson MA, Wasserfall CH, et al. Novel synthesis of cerium oxide nanoparticles for free radical scavenging. *Nanomedicine (Lond)*. 2007;2(3):325-32.
42. Park B, Donaldson K, Duffin R, Tran L, Kelly F, Mudway I, et al. Hazard and risk assessment of a nanoparticulate cerium oxide-based diesel fuel additive - a case study. *Inhal Toxicol*. 2008;20(6):547-66.
43. De Marzi L, Monaco A, De Lapuente J, Ramos D, Borrás M, Di Gioacchino M, et al. Cytotoxicity and genotoxicity of ceria nanoparticles on different cell lines in vitro. *Int J Mol Sci*. 2013;14(2):3065-77.
44. Das M, Patil S, Bhargava N, Kang J-F, Riedel LM, Seal S, et al. Auto-catalytic ceria nanoparticles offer neuroprotection to adult rat spinal cord neurons. *Biomaterials*. 2007;28(10):1918-25.
45. Babu KS, Anandkumar M, Tsai TY, Kao TH, Inbaraj BS, Chen BH. Cytotoxicity and antibacterial activity of gold-supported cerium oxide nanoparticles. *International journal of nanomedicine*. 2014;9:5515-31.
46. Limbach LK, Bereiter R, Muller E, Krebs R, Galli R, Stark WJ. Removal of oxide nanoparticles in a model wastewater treatment plant: influence of agglomeration and surfactants on clearing efficiency. *Environmental science & technology*. 2008;42(15):5828-33.
47. Van Hoecke K, Quik JT, Mankiewicz-Boczek J, De Schamphelaere KA, Elsaesser A, Van der Meeren P, et al. Fate and effects of CeO₂ nanoparticles in aquatic ecotoxicity tests. *Environmental science & technology*. 2009;43(12):4537-46.
48. Lin W, Huang Y-w, Zhou X-D, Ma Y. Toxicity of Cerium Oxide Nanoparticles in Human Lung Cancer Cells. *International Journal of Toxicology*. 2006;25(6):451-7.
49. Pelletier DA, Suresh AK, Holton GA, McKeown CK, Wang W, Gu B, et al. Effects of Engineered Cerium Oxide Nanoparticles on Bacterial Growth and Viability. *Applied and Environmental Microbiology*. 2010;76(24):7981-9.
50. Zhang W, Zhang W, Mujumdar AS, Huang L. Progress in Drying Technology for Nanomaterials AU - Wang, Baohe. *Drying Technology*. 2005;23(1-2):7-32.
51. Channei D, Phanichphant S, Nakaruk A, Mofarah SS, Koshy P, Sorrell CC. Aqueous and Surface Chemistries of Photocatalytic Fe-Doped CeO₂ Nanoparticles. *Catalysts*. 2017;7(2):45.
52. Korsvik C, Patil S, Seal S, Self WT. Superoxide dismutase mimetic properties exhibited by vacancy engineered ceria nanoparticles. *Chemical communications (Cambridge, England)*. 2007(10):1056-8.
53. Aguilera-Correa JJ, Garcia-Casas A, Mediero A, Romera D, Mulero F, Cuevas-López I, et al. A New Antibiotic-Loaded Sol-Gel Can Prevent Bacterial Prosthetic Joint Infection: From in vitro Studies to an in vivo Model. *Frontiers in Microbiology*. 2020;10(2935).

54. Crémet L, Corvec S, Bémer P, Bret L, Lebrun C, Lesimple B, et al. Orthopaedic-implant infections by *Escherichia coli*: Molecular and phenotypic analysis of the causative strains. *Journal of Infection*. 2012;64(2):169-75.
55. Olivares E, Badel-Berchoux S, Provot C, Prévost G, Bernardi T, Jehl F. Clinical Impact of Antibiotics for the Treatment of *Pseudomonas aeruginosa* Biofilm Infections. *Frontiers in Microbiology*. 2020;10(2894).
56. Mahdi AA, Al-Salmani TS, Al-Qaisi MM. The Novel Role of Healing from Bacterial Infections of Lower Limb Open Fractures by X-Ray Exposure. *International Journal of Microbiology*. 2020;2020:3129356.
57. Davidson DJ, Spratt D, Liddle AD. Implant materials and prosthetic joint infection: the battle with the biofilm. *EFORT Open Reviews*. 2019;4(11):633-9.
58. Gritsch L, Lovell C, Goldmann WH, Boccaccini AR. Fabrication and characterization of copper(II)-chitosan complexes as antibiotic-free antibacterial biomaterial. *Carbohydr Polym*. 2018;179:370-8.
59. Clais S, Boulet G, Van kerckhoven M, Lanckacker E, Delputte P, Maes L, et al. Comparison of viable plate count, turbidity measurement and real-time PCR for quantification of *Porphyromonas gingivalis*. *Letters in Applied Microbiology*. 2015;60(1):79-84.
60. Lapa A, Cresswell M, Campbell I, Jackson P, Goldmann W, Detsch R, et al. Correction: Ga and Ce ion-doped phosphate glass fibres with antibacterial properties and their composite for wound healing applications. *Journal of Materials Chemistry B*. 2019;7.
61. Phoka S, Laokul P, Swatsitang E, Promarak V, Seraphin S, Maensiri S. Synthesis, structural and optical properties of CeO₂ nanoparticles synthesized by a simple polyvinyl pyrrolidone (PVP) solution route. *Materials Chemistry and Physics*. 2009;115(1):423-8.
62. Baqer AA, Matori KA, Al-Hada NM, Shaari AH, Saion E, Chyi JLY. Effect of polyvinylpyrrolidone on cerium oxide nanoparticle characteristics prepared by a facile heat treatment technique. *Results in Physics*. 2017;7:611-9.
63. Sifontes AB, Rosales M, Mendez FJ, Oviedo O, Zoltan T. Effect of calcination temperature on structural properties and photocatalytic activity of ceria nanoparticles synthesized employing chitosan as template. *Journal of Nanomaterials*. 2013.
64. Alpaslan E, Geilich BM, Yazici H, Webster TJ. pH-Controlled Cerium Oxide Nanoparticle Inhibition of Both Gram-Positive and Gram-Negative Bacteria Growth. *Sci Rep*. 2017;7:45859-.
65. Sirelkhatim A, Mahmud S, Seeni A, Kaus NHM, Ann LC, Bakhori SKM, et al. Review on Zinc Oxide Nanoparticles: Antibacterial Activity and Toxicity Mechanism. *Nano-Micro Letters*. 2015;7(3):219-42.
66. Thakur N, Manna P, Das J. Synthesis and biomedical applications of nanoceria, a redox active nanoparticle. *Journal of Nanobiotechnology*. 2019;17(1):84.
67. Farahmandjou M, Zarinkamar M, Firoozabadi T. Synthesis of Cerium Oxide (CeO₂) nanoparticles using simple CO-precipitation method. *Revista Mexicana de Fisica*. 2016;62:496-9.
68. Prabakaran D, Sadaiyandi K, Mahendran M, Sagadevan S. Structural, Optical, Morphological and Dielectric Properties of Cerium Oxide Nanoparticles. *Materials Research-ibero-american Journal of Materials*. 2016;19:478-82.
69. Caputo F, Mameli M, Sienkiewicz A, Licocchia S, Stellacci F, Ghibelli L, et al. A novel synthetic approach of cerium oxide nanoparticles with improved biomedical activity. *Sci Rep*. 2017;7(1):4636.
70. Dao NN, Luu MD, Nguyen QK, Kim BS. UV absorption by cerium oxide nanoparticles/epoxy composite thin films. *Advances in Natural Sciences: Nanoscience and Nanotechnology*. 2011;2(4):045013.

71. Ren Z, Peng F, Li J, Liang X, Chen B. Morphology-Dependent Properties of Cu/CeO₂ Catalysts for the Water-Gas Shift Reaction. *Catalysts*. 2017;7:48.
72. Tsunekawa S, Wang J-T, Kawazoe Y, Kasuya A. Blueshifts in the ultraviolet absorption spectra of cerium oxide nanocrystallites. *Journal of Applied Physics*. 2003;94:3654-6.
73. Gillen R, Clark S, Robertson J. Nature of the electronic band gap in lanthanide oxides. *Physical Review B*. 2012;87.
74. Skorodumova N, Ahuja R, Simak SI, Abrikosov IA, Johansson B, Lundqvist B. Electronic, bonding, and optical properties of CeO₂ and Ce₂O₃ from first principles. *Phys Rev B*. 2001;64:1-9.
75. Burroughs P, Hamnett A, Orchard AF, Thornton G. Satellite structure in the X-ray photoelectron spectra of some binary and mixed oxides of lanthanum and cerium. *Journal of the Chemical Society, Dalton Transactions*. 1976(17):1686-98.
76. Janoš P, Hladík T, Kormunda M, Ederer J, Šťastný M. Thermal Treatment of Cerium Oxide and Its Properties: Adsorption Ability versus Degradation Efficiency. *Advances in Materials Science and Engineering*. 2014;2014:706041.
77. Zhang J, Wong H, Yu D, Kakushima K, Iwai H. X-ray photoelectron spectroscopy study of high-k CeO₂/La₂O₃ stacked dielectrics. *AIP Advances*. 2014;4(11):117117.
78. Holgado JP, Munuera G, Espinós JP, González-Elipe AR. XPS study of oxidation processes of CeO_x defective layers. *Applied Surface Science*. 2000;158(1):164-71.
79. Holgado JP, Alvarez R, Munuera G. Study of CeO₂ XPS spectra by factor analysis: reduction of CeO₂. *Applied Surface Science*. 2000;161:301.
80. Shah V, Shah S, Shah H, Rispoli FJ, McDonnell KT, Workeneh S, et al. Antibacterial activity of polymer coated cerium oxide nanoparticles. *PLoS One*. 2012;7(10):e47827.
81. Wang Q, Perez JM, Webster TJ. Inhibited growth of *Pseudomonas aeruginosa* by dextran- and polyacrylic acid-coated ceria nanoparticles. *International journal of nanomedicine*. 2013;8:3395-9.
82. Xia T, Kovoichich M, Brant J, Hotze M, Sempf J, Oberley T, et al. Comparison of the abilities of ambient and manufactured nanoparticles to induce cellular toxicity according to an oxidative stress paradigm. *Nano Lett*. 2006;6(8):1794-807.
83. Xia T, Kovoichich M, Liang M, Mädler L, Gilbert B, Shi H, et al. Comparison of the mechanism of toxicity of zinc oxide and cerium oxide nanoparticles based on dissolution and oxidative stress properties. *ACS Nano*. 2008;2(10):2121-34.
84. Burello E, Worth AP. A theoretical framework for predicting the oxidative stress potential of oxide nanoparticles. *Nanotoxicology*. 2011;5(2):228-35.
85. Hajipour MJ, Fromm KM, Akbar Ashkarran A, Jimenez de Aberasturi D, Larramendi IRd, Rojo T, et al. Antibacterial properties of nanoparticles. *Trends in biotechnology*. 2012;30(10):499-511.
86. Farias IAP, Santos CCLd, Sampaio F, Correia b. Antimicrobial Activity of Cerium Oxide Nanoparticles on Opportunistic Microorganisms: A Systematic Review. *BioMed Research International*. 2018;2018:14.

Figures

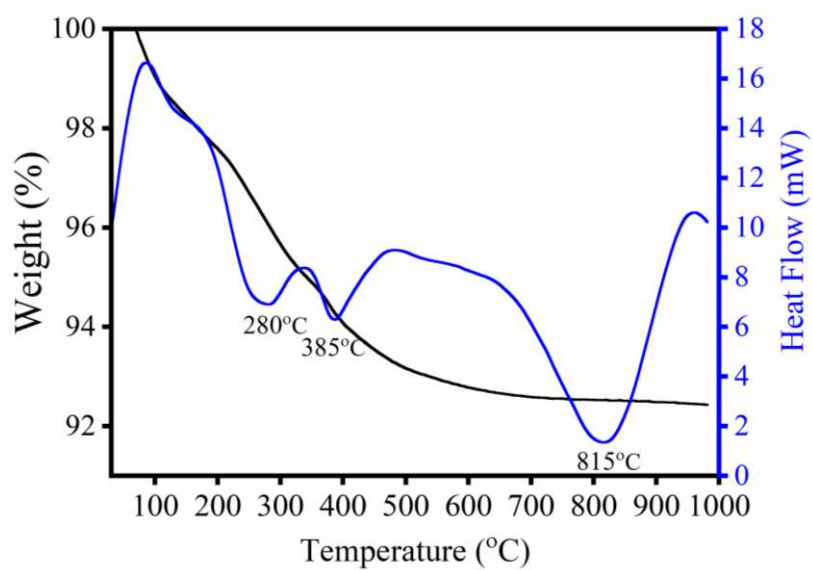


Figure 1 - Simultaneous Thermal Analysis spectrum of FUNP nanoparticles depicting three critical endothermic peaks at 280 °C, 385 °C, and 815 °C is signifying potential structural changes concerning the $\text{Ce}^{3+}:\text{Ce}^{4+}$ ratio.

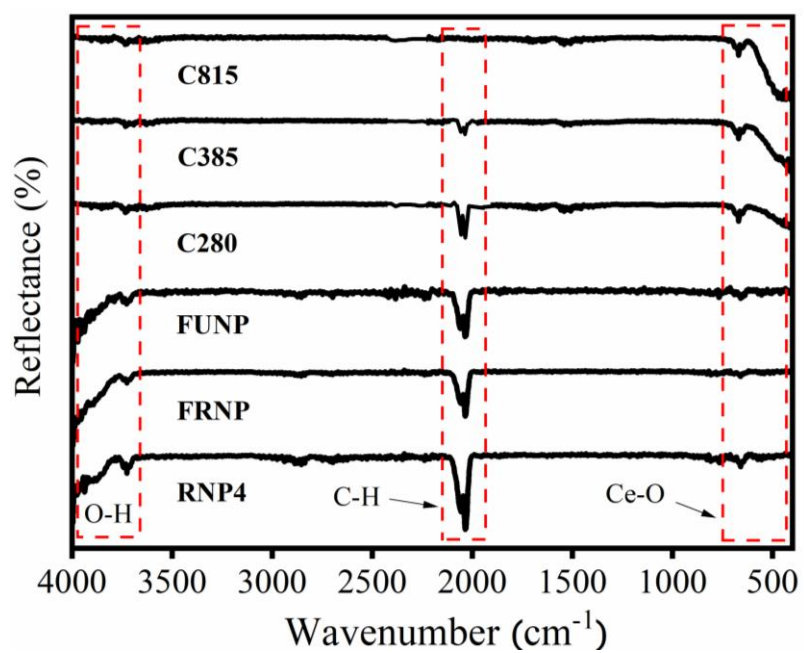


Figure 2 - Vertex 70 FTIR pattern for cerium oxide nanoparticles from 4000 cm⁻¹ to 400 cm⁻¹

¹. The operating parameters consisted of a total of 32 scans at a resolution of 4 cm⁻¹.

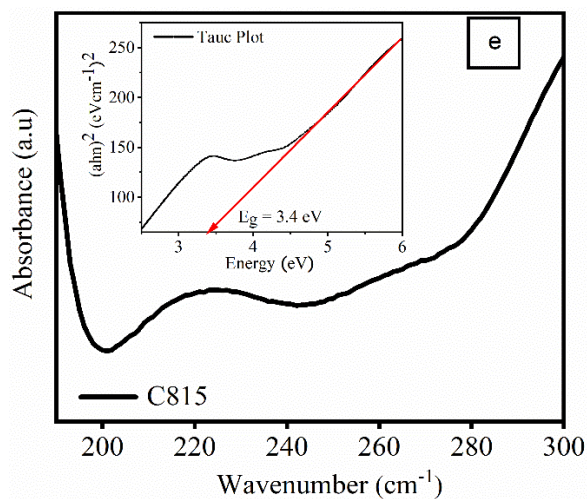
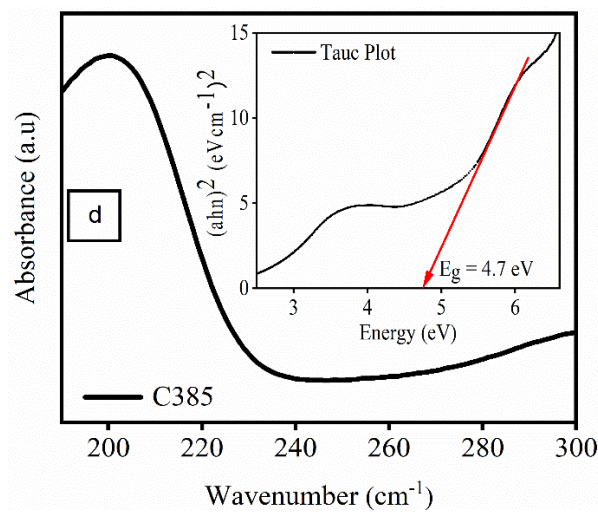
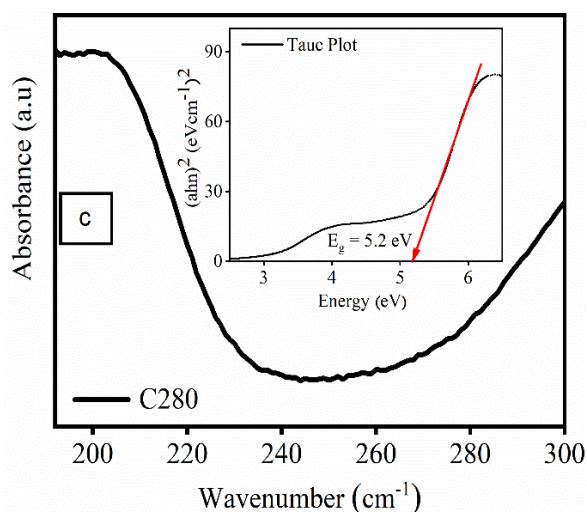
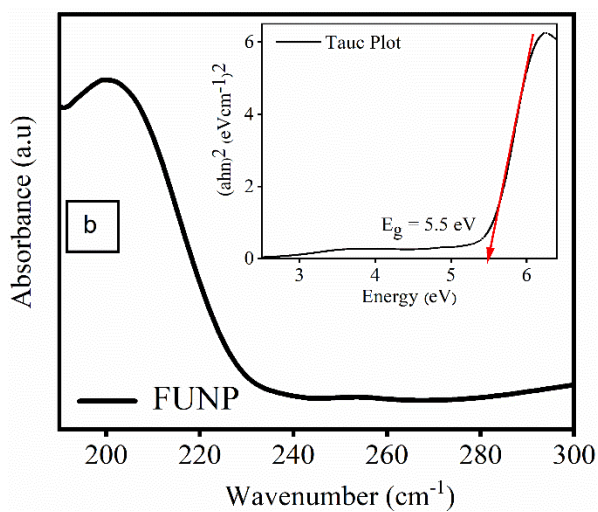
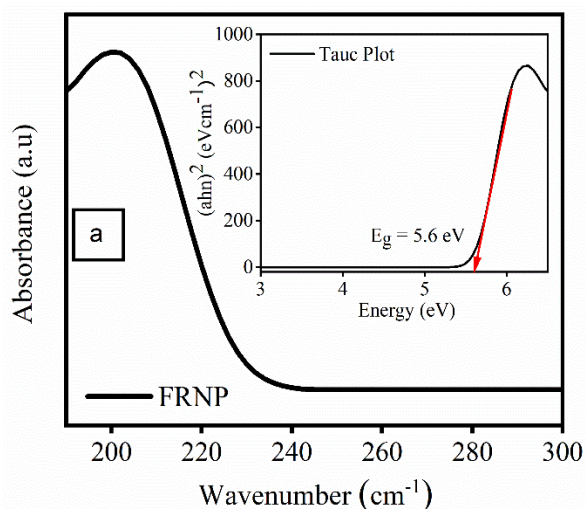


Figure 3 - UV-vis absorbance spectra obtained from cerium oxide nanoparticles concentrations of 0.5 mg/ml and corresponding Tauc Plots, (a) FRNP, (b) FUNP, (c) C280, (d) C385 and (e) C815.

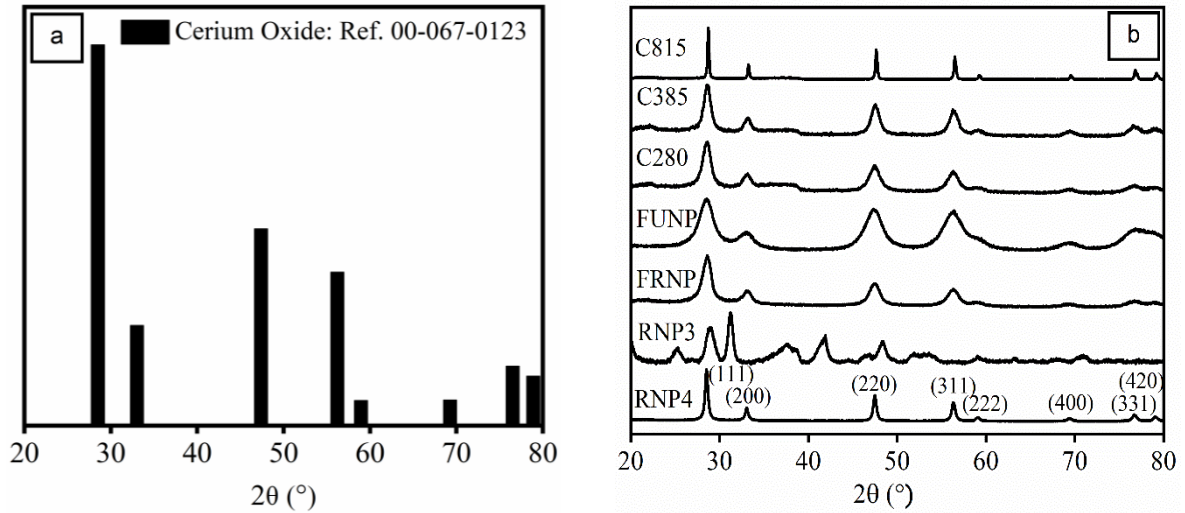


Figure 4 - X-ray diffraction patterns of cerium oxide nanoparticles, 2θ scanning range was 20° to 80° at a scan speed of 5s and increment of 0.03° ; (a) reference pattern of cerium oxide nanoparticles JCPDS 00-067-0123; (b) commercial and synthesised cerium oxide nanoparticles calcined at 280°C , 385°C and 815°C .

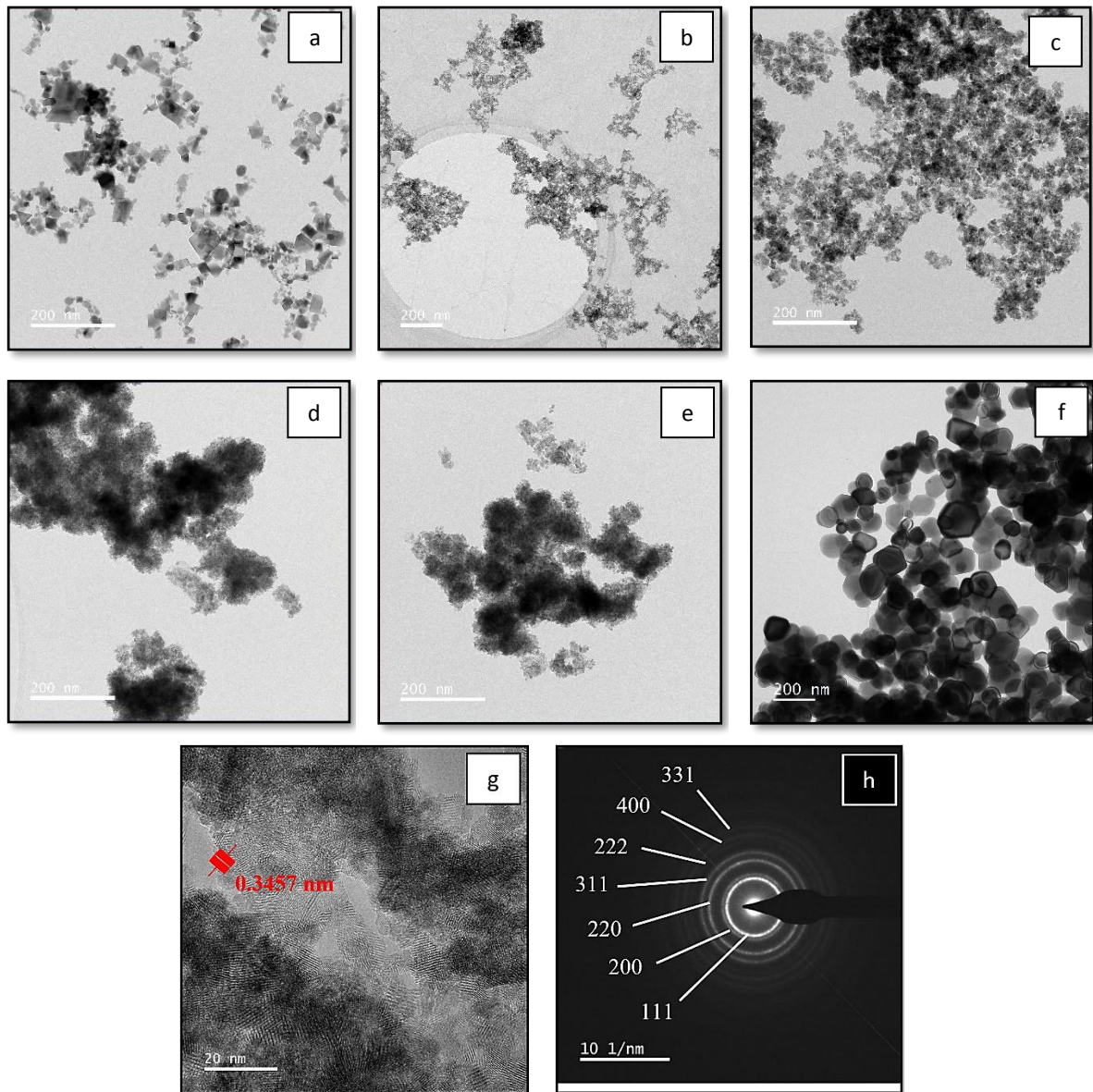


Figure 5 - Comparison of Titan Themis Cubed 300 TEM images of nanoparticles calcined at various temperatures (a) RNP4, (b) FRNP, (c) FUNP, (d) C280, (e) C385, (f) C815, (g) HRTEM image of FUNP and (h) SAED of FRNP.

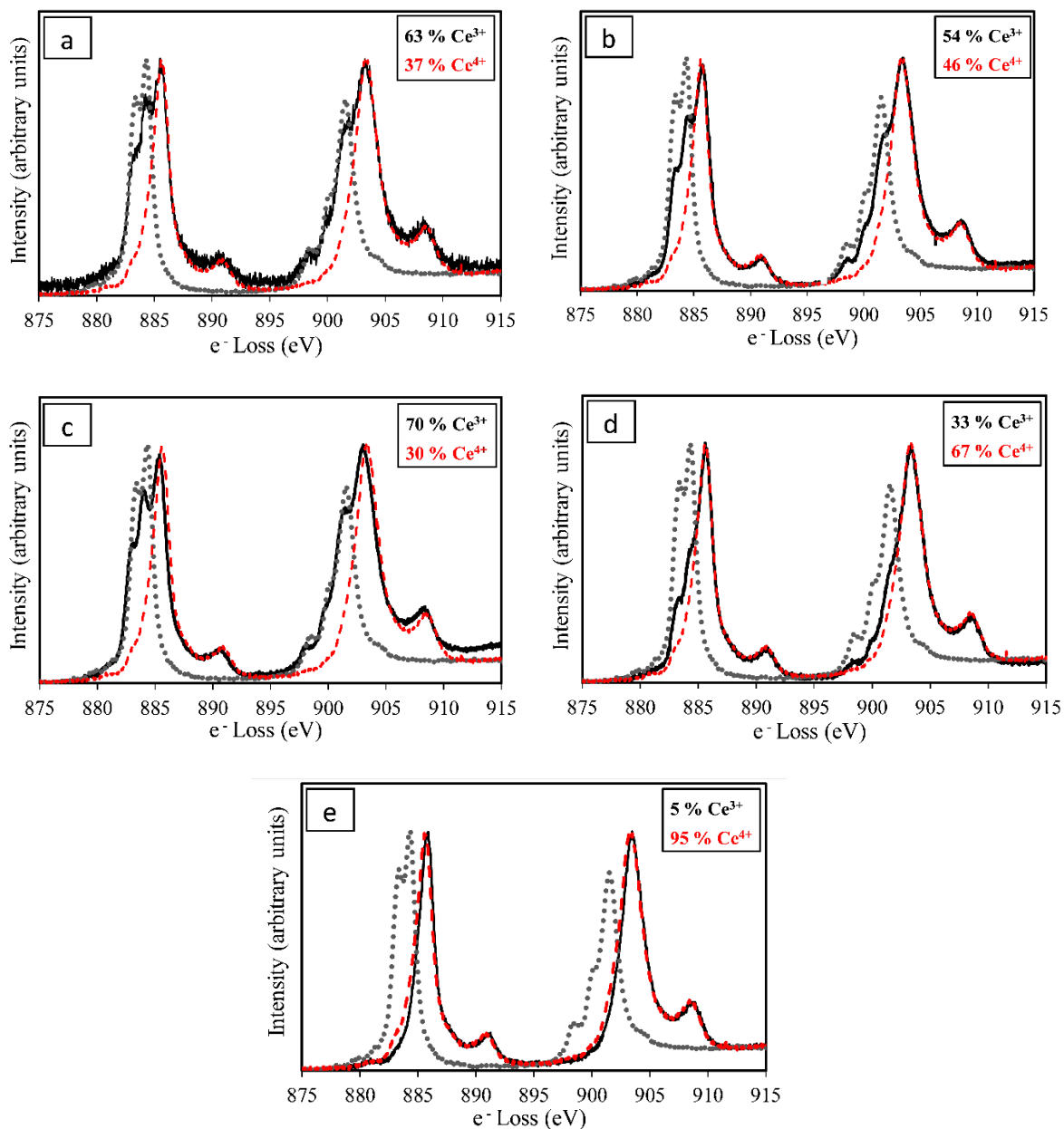


Figure 6 - Normalized EELs spectra depicting the presence of dual oxidation states. (a) FRNP, (b) FUNP, (c) C280, (d) C385 and (e) C815. Compared with Ce^{3+} (grey) and Ce^{4+} (red) standards.

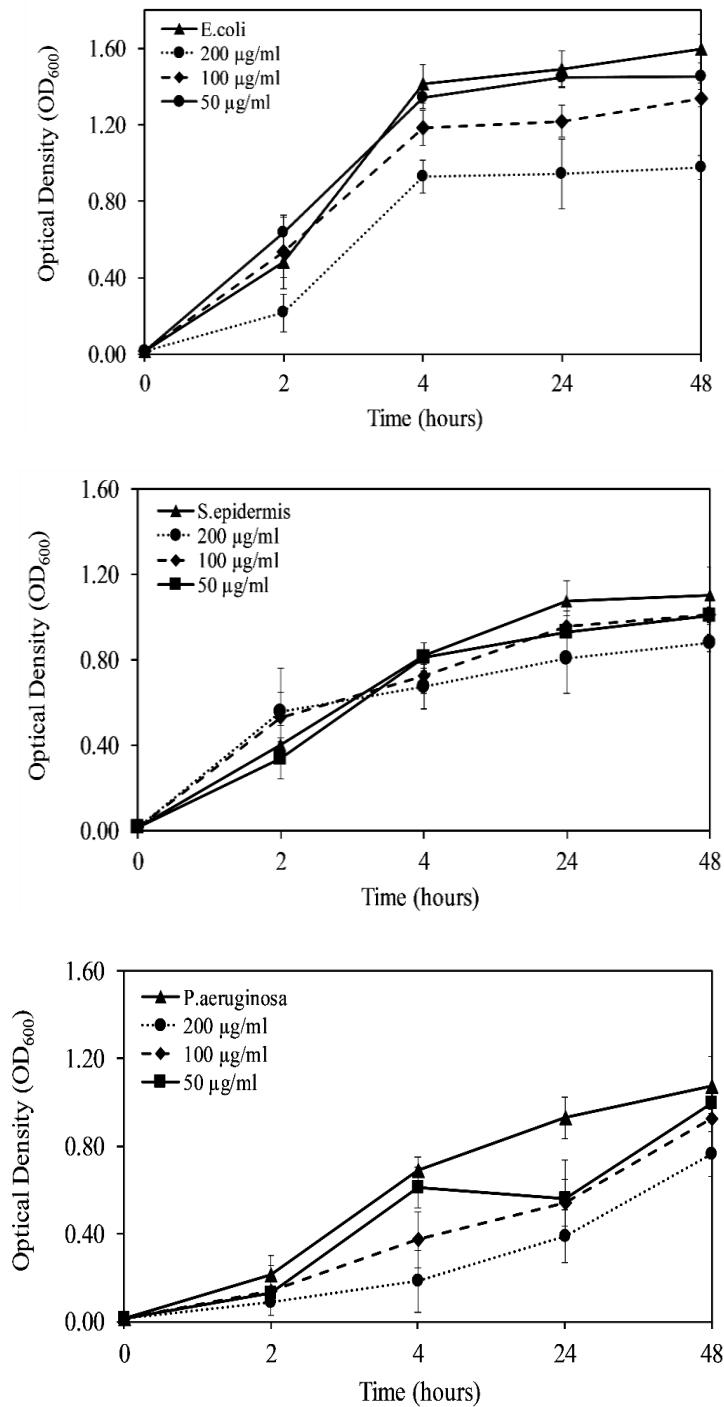


Figure 7 - Optical density of the bacteria characterising the antibacterial properties of FRNP after direct incubation with *Escherichia coli*, *Pseudomonas aeruginosa* and *Staphylococcus epidermidis* for 48 hours.

Figures

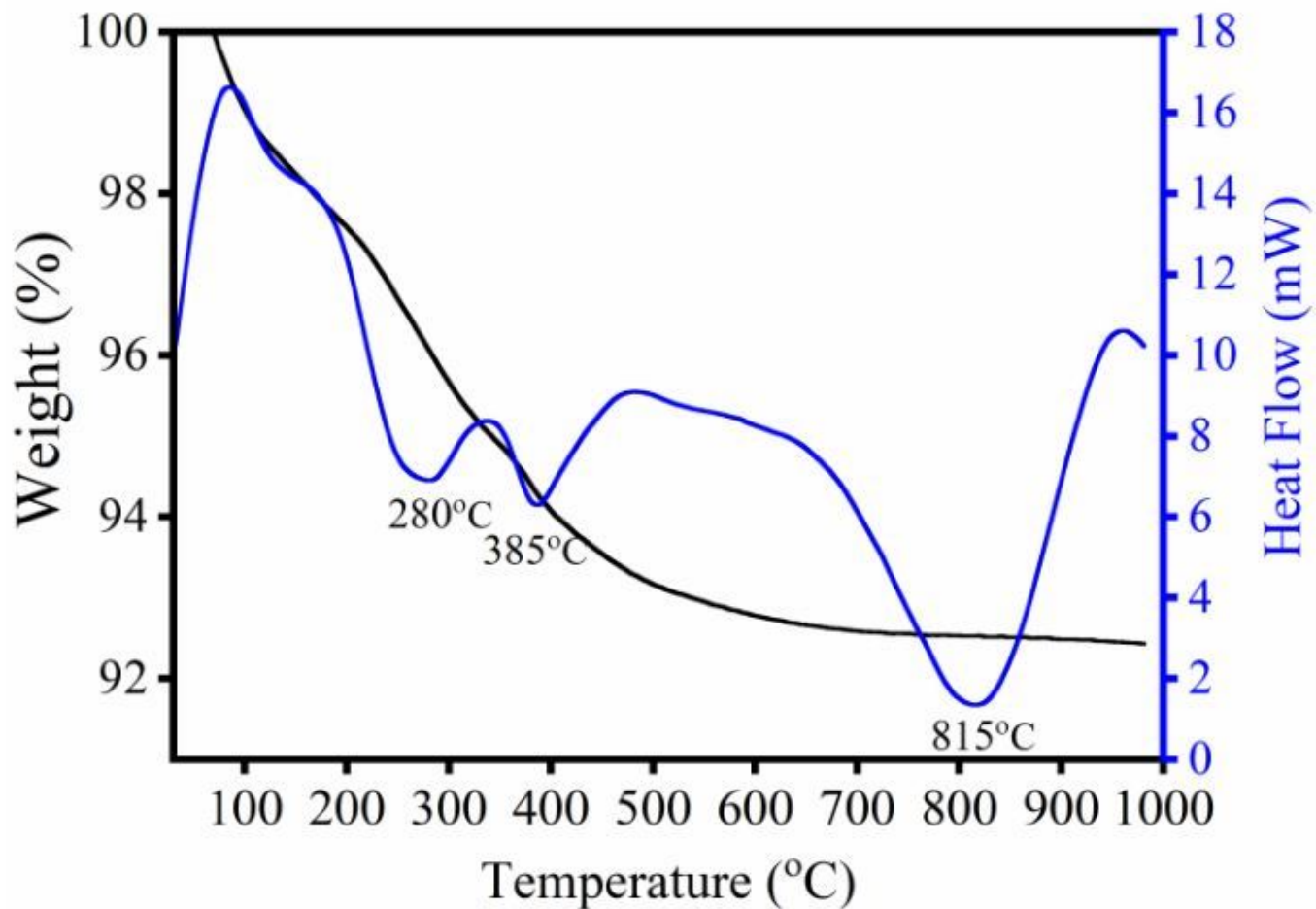


Figure 1

Simultaneous Thermal Analysis spectrum of FUNP nanoparticles depicting three critical endothermic peaks at 280 °C, 385 °C, and 815 °C is signifying potential structural changes concerning the Ce³⁺:Ce⁴⁺ ratio.

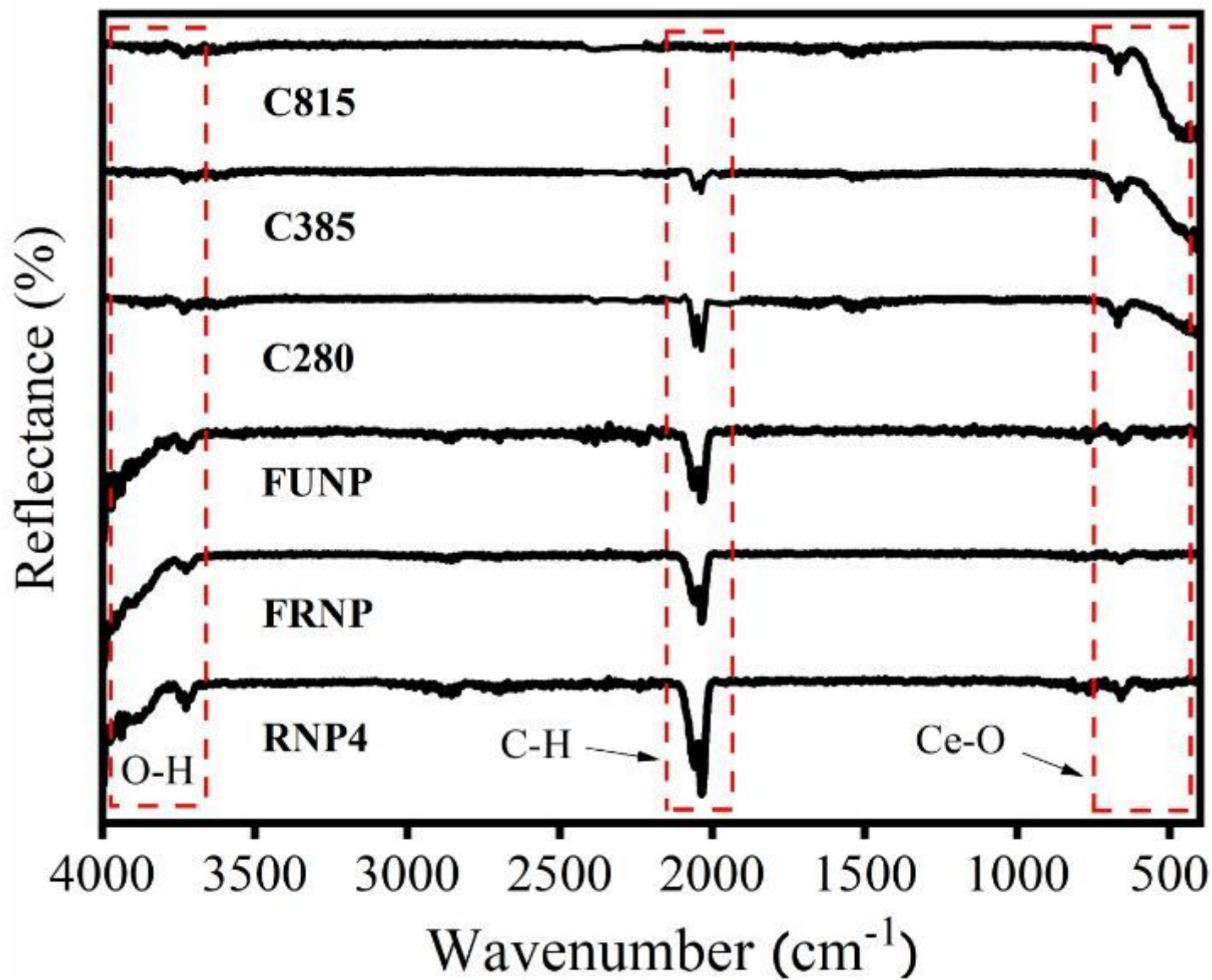


Figure 2

Vertex 70 FTIR pattern for cerium oxide nanoparticles from 4000 cm⁻¹ to 400 cm⁻¹. The operating parameters consisted of a total of 32 scans at a resolution of 4 cm⁻¹.

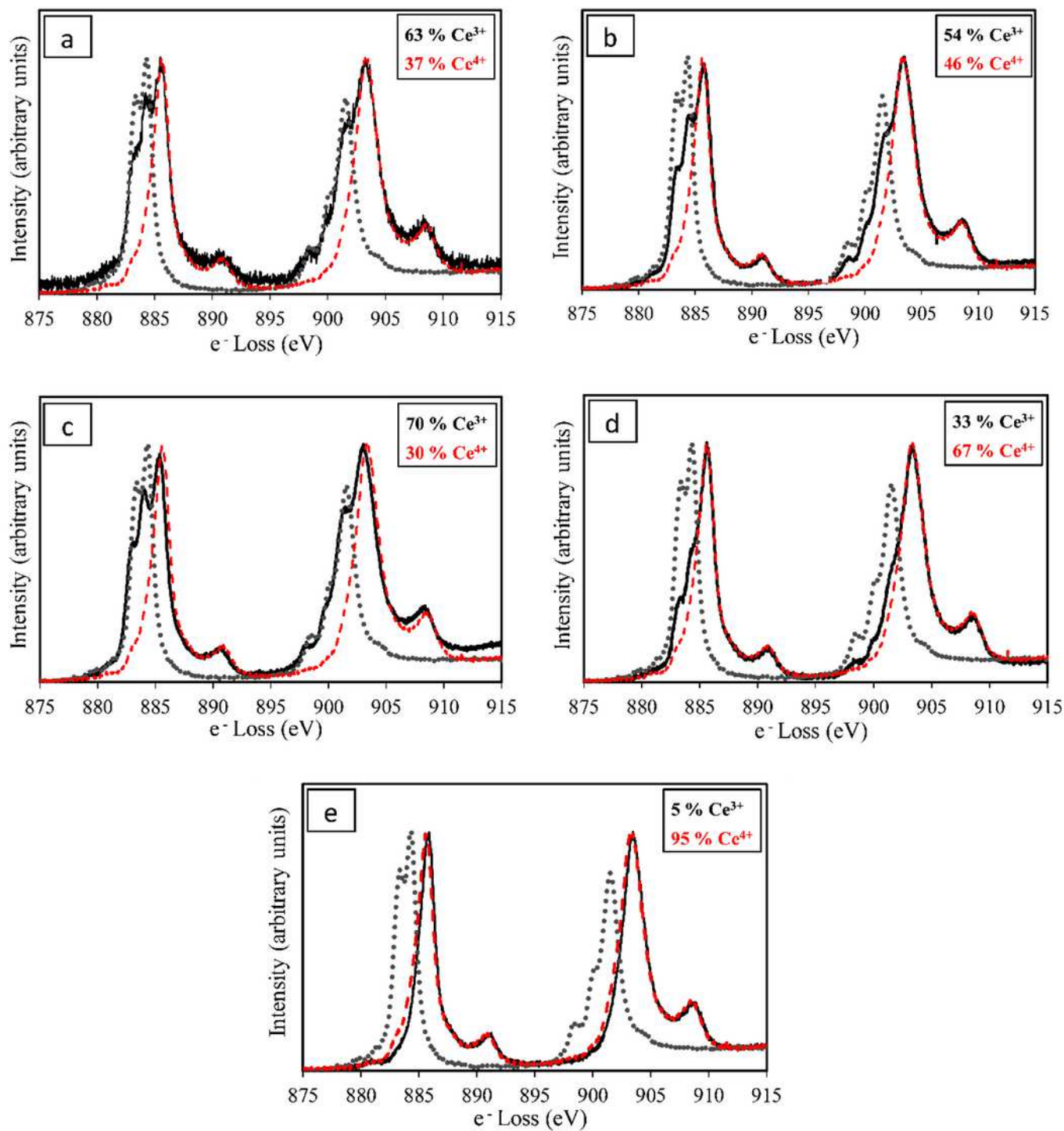


Figure 3

UV-vis absorbance spectra obtained from cerium oxide nanoparticles concentrations of 0.5 mg/ml and corresponding Tauc Plots, (a) FRNP, (b) FUNP, (c) C280, (d) C385 and (e) C815.

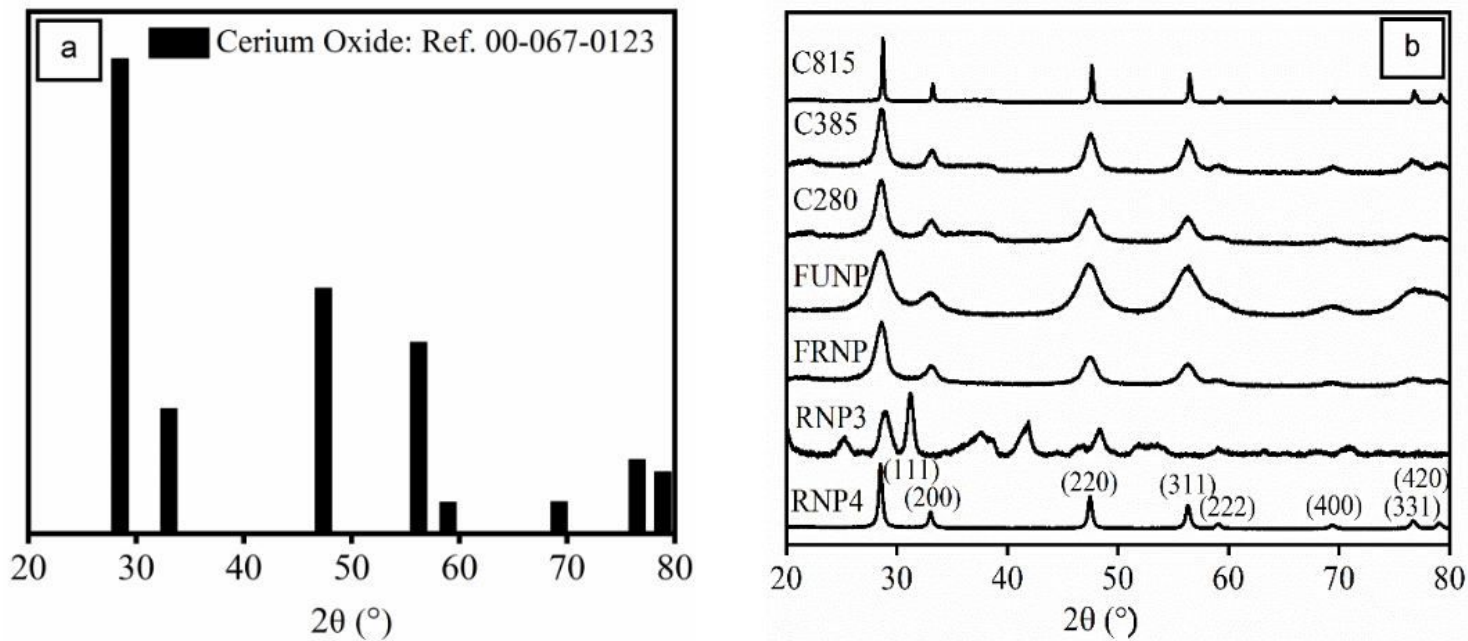


Figure 4

X-ray diffraction patterns of cerium oxide nanoparticles, 2θ scanning range was 20° to 80° at a scan speed of 5s and increment of 0.03° ; (a) reference pattern of cerium oxide nanoparticles JCPDS 00-067-0123; (b) commercial and synthesised cerium oxide nanoparticles calcined at 280°C , 385°C and 815°C .

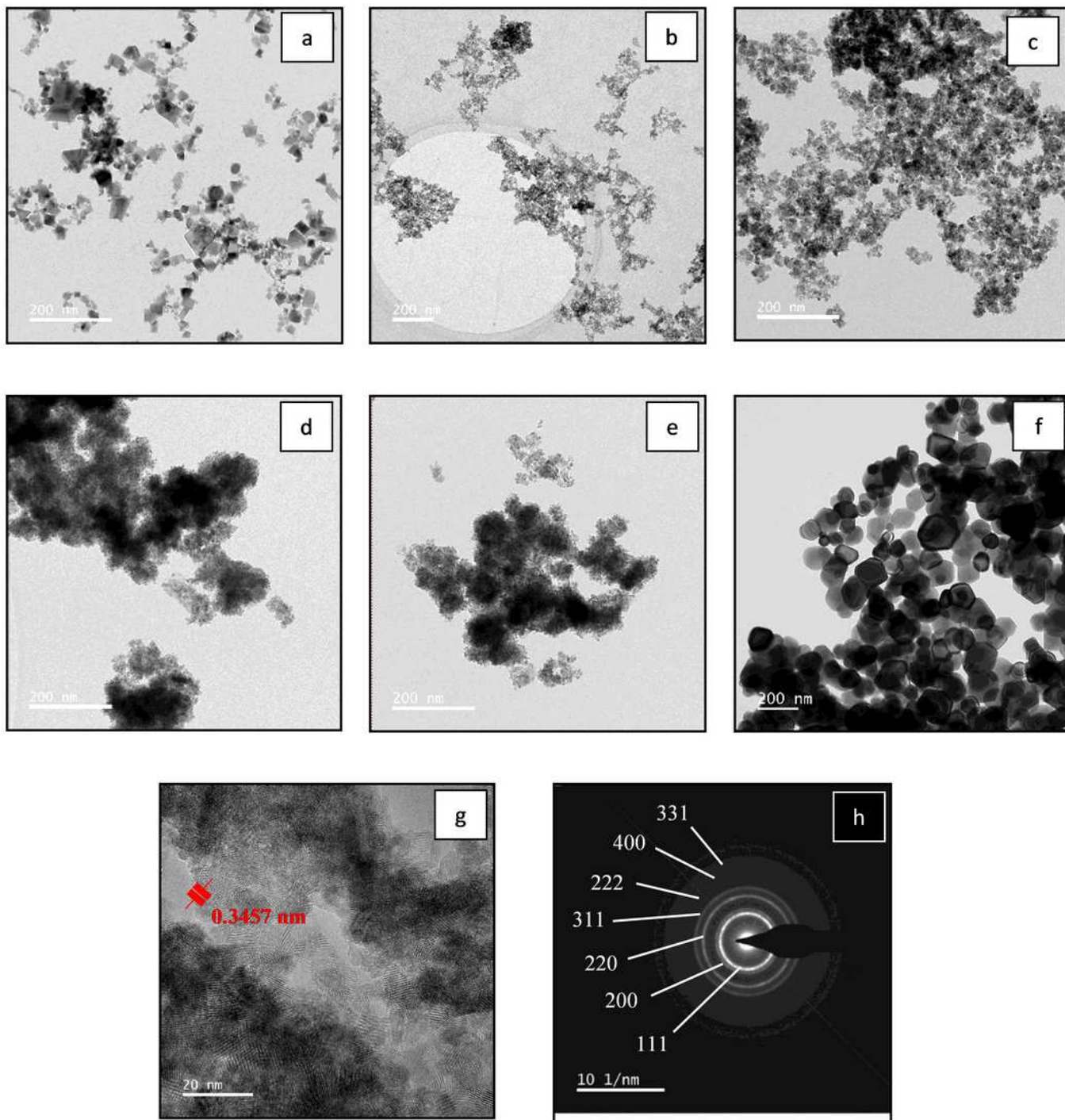


Figure 5

Comparison of Titan Themis Cubed 300 TEM images of nanoparticles calcined at various temperatures (a) RNP4, (b) FRNP, (c) FUNP, (d) C280, (e) C385, (f) C815, (g) HRTEM image of FUNP and (h) SAED of FRNP.

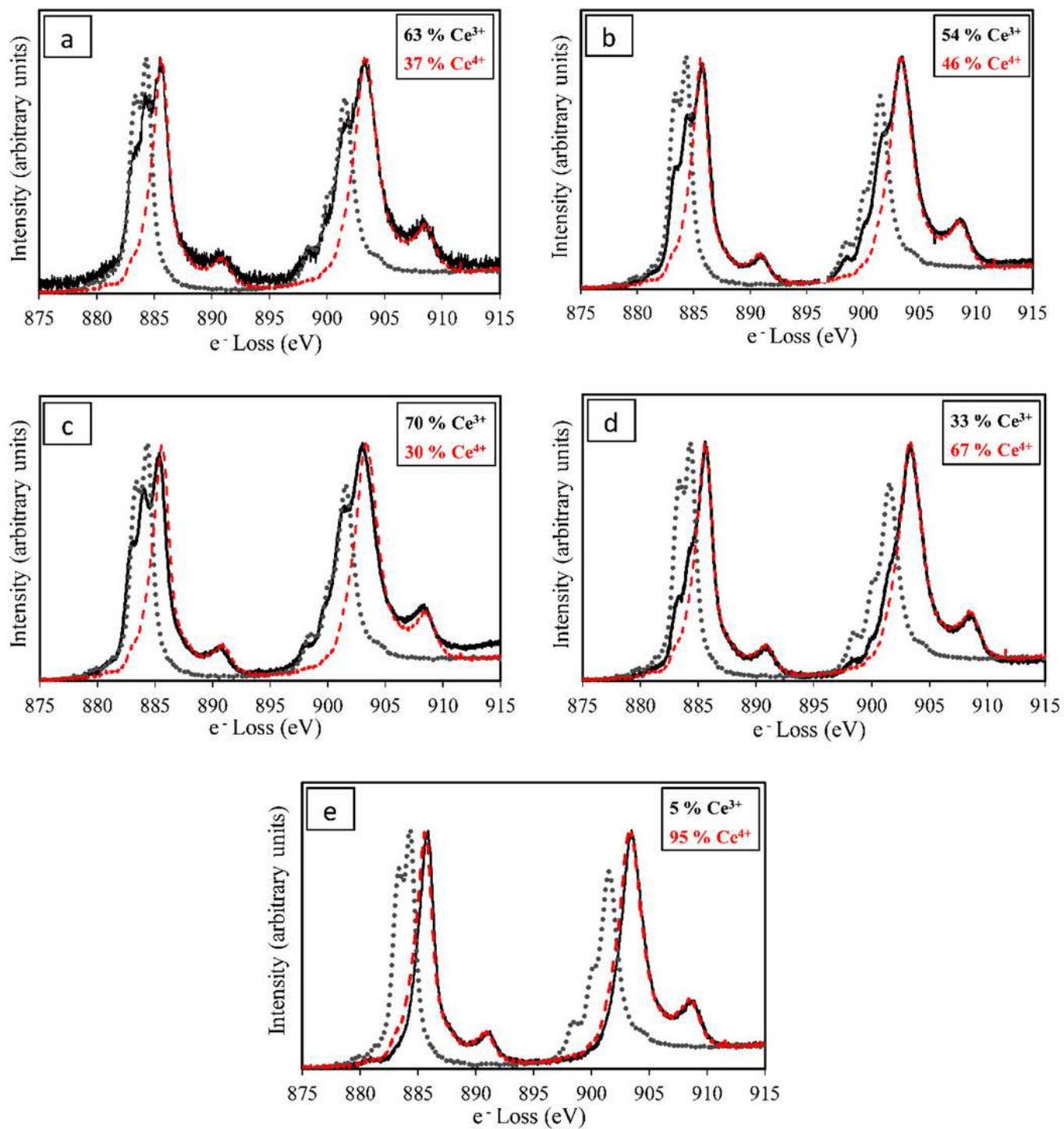


Figure 6

Normalized EELS spectra depicting the presence of dual oxidation states. (a) FRNP, (b) FUNP, (c) C280, (d) C385 and (e) C815. Compared with Ce^{3+} (grey) and Ce^{4+} (red) standards.

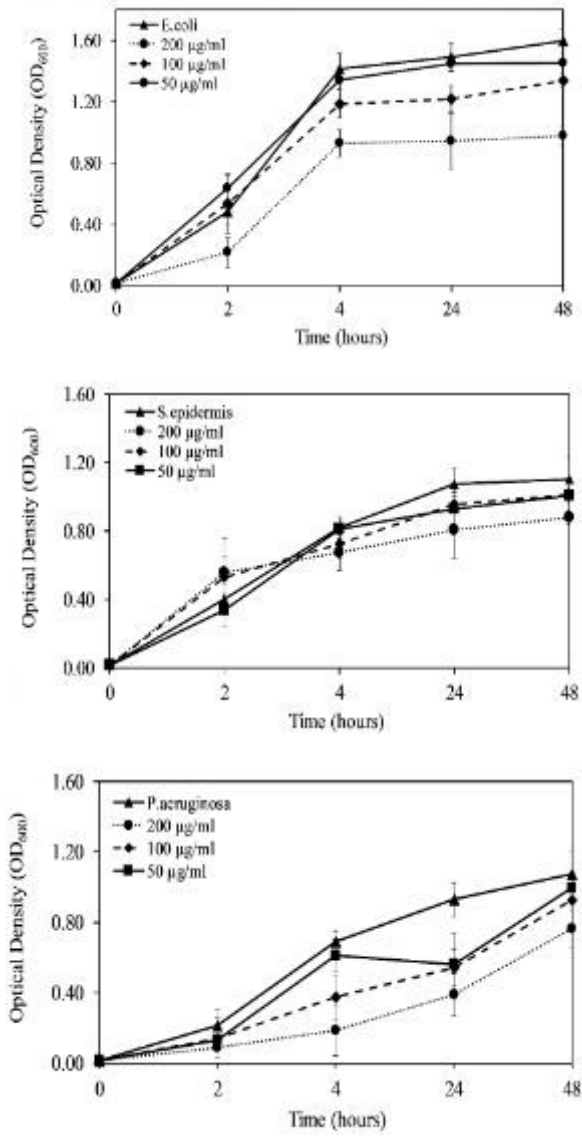


Figure 7

Optical density of the bacteria characterising the antibacterial properties of FRNP after direct incubation with *Escherichia coli*, *Pseudomonas aeruginosa* and *Staphylococcus epidermidis* for 48 hours.